

Schaye 2001). A robust prediction of cosmological simulations is that most of these ‘missing baryons’ reside in a gas phase with densities $n_{\text{H}} \sim 10^{-6} - 10^{-5} \text{ cm}^{-3}$ that, as a result of the formation of structure in the Universe, has been shock-heated to temperatures $T \gtrsim 10^5 \text{ K}$ (e.g. Cen & Ostriker 1999; Davé et al. 2001; Bertone et al. 2008). Along with gravitational shock-heating, feedback processes such as supernova (SN) explosions and outflows driven by active galactic nuclei (AGN) have been shown to significantly contribute to the mass in this diffuse, warm-hot gas phase at low redshift (e.g. Tepper-García et al. 2012).

So far, attempts to trace shock-heated diffuse gas at low redshift, and to constrain its baryon content, have mainly relied on the detection of absorption by five-times ionised oxygen ($\text{O}\,\text{vi}$) in the UV spectra of distant point-like sources (e.g. quasars, QSOs; Tripp et al. 2000; Richter et al. 2004; Danforth et al. 2006; Danforth & Shull 2008; Thom & Chen 2008b; Tripp et al. 2008; Danforth et al. 2010; Prochaska et al. 2011). However, because $\text{O}\,\text{vi}$ may be produced both by photo-ionisation in gas at $T \sim 10^4 \text{ K}$ and by collisional ionisation in gas at $T \approx 3 \times 10^5 \text{ K}$, and because the metals may well be poorly mixed on small scales (Schaye et al. 2007), the interpretation of intervening $\text{O}\,\text{vi}$ absorbers and their status as tracers of shock-heated gas is still controversial, as shown by both observational (Thom & Chen 2008a; Tripp et al. 2008; Danforth & Shull 2008) and theoretical studies (e.g. Oppenheimer & Davé 2009; Tepper-García et al. 2011; Smith et al. 2011; Cen 2012). Besides $\text{O}\,\text{vi}$, broad ($b_{\text{H}\,\text{I}} \geq 40 \text{ km s}^{-1}$) and shallow ($\tau_0(\text{H}\,\text{I}) \lesssim 0.1$) $\text{Ly}\alpha$ absorption features, the so-called Broad $\text{Ly}\alpha$ Absorbers (BLAs; Richter et al. 2006), have been considered as a means to detect diffuse warm-hot gas at low redshift (Sembach et al. 2004; Richter et al. 2004; Williger et al. 2006; Lehner et al. 2007; Danforth et al. 2010; Tepper-García et al. 2012). However, BLAs are difficult to identify in the UV spectra of QSOs because of the limited signal-to-noise (S/N) and spectral resolution of data obtained with current space-based UV spectrographs.

An alternative to $\text{O}\,\text{vi}$ and BLAs as tracers of shock-heated gas might be offered by seven-times ionised neon ($\text{Ne}\,\text{viii}$). Neon is the fifth most abundant element in the Universe,¹ and this particular ionisation state has two resonant transitions with rest-frame wavelengths in the extreme ultra-violet (EUV) at wavelengths 770.41 Å and 780.32 Å (e.g. Verner et al. 1994), which are redshifted into the COS spectral range at $z \gtrsim 0.5$. The $\text{Ne}\,\text{viii}$ ionisation fraction in collisional ionisation equilibrium (CIE) is highest at temperatures $T \approx 5 \times 10^5 \text{ K}$ (e.g. Sutherland & Dopita 1993).

To date, though, only a handful of intervening (as opposed to ‘proximate to the QSO’) $\text{Ne}\,\text{viii}$ absorbers have been identified in UV absorption spectra at redshifts $z < 1$ (Savage et al. 2005; Narayanan et al. 2009, 2011; Tripp et al. 2011; Meiring et al. 2012). Interestingly, all these absorbers have similar strengths, with column densities $N_{\text{Ne}\,\text{viii}} \sim 10^{14} \text{ cm}^{-2}$, and they all show a simple kinematic structure (at the given sensitivity and spectral resolution), thus suggesting that the observed $\text{Ne}\,\text{viii}$ absorption is produced in gas under rather uniform physical conditions (but see Tripp et al. 2011). In particular, the narrow range of measured temperatures ($\log_{10}(T/\text{K}) \approx 5.4 - 5.7$) indicates, first, that $\text{Ne}\,\text{viii}$ absorbers are very sensitive probes of the thermal state of the absorbing gas; and second, that $\text{Ne}\,\text{viii}$ absorbers are reliable tracers of gas at $T \approx 5 \times 10^5 \text{ K}$ (Savage et al. 2005, but see Oppenheimer & Schaye 2013a who argue that $\text{Ne}\,\text{viii}$ absorbers may trace fossil AGN proximity zones). Furthermore, their relatively high hydrogen column densities ($N_{\text{H}} \sim 10^{19} - 10^{20} \text{ cm}^{-2}$)

¹ After hydrogen, helium, oxygen and carbon.

suggest that they contain a substantial amount of baryons (Savage et al. 2005; Narayanan et al. 2009). In view of these findings, $\text{Ne}\,\text{viii}$ absorbers indeed seem a promising tool in the search for warm-hot, diffuse gas and the ‘missing baryons’ in the low redshift Universe.

A clear link between the intervening $\text{Ne}\,\text{viii}$ absorbers and this peculiar gas phase has, however, not as yet been observationally established due to the current small number of detections, and support from the theoretical side is hence called for. This is the motivation for the present paper.

Here, we investigate in detail the physical conditions of gas producing $\text{Ne}\,\text{viii}$ absorption at low redshift following two rather independent and complementary approaches. First, we make use of a cosmological simulation that samples a representative volume of the universe at $z = 0.5$ and which includes many of the physical processes believed to be important for the production and distribution of metals in the Universe. From this simulation we extract the distribution of densities and temperatures, the baryon content and the level of enrichment of a statistically significant sample of $\text{Ne}\,\text{viii}$ absorbers. Additionally, we use this sample to make predictions for two canonical absorption-line statistical quantities: the distribution of $\text{Ne}\,\text{viii}$ column densities and the number of $\text{Ne}\,\text{viii}$ absorbers of a given strength per unit redshift. Second, we develop an analytic model to predict standard observables (i.e. $\text{Ne}\,\text{viii}$ column density, $\text{Ne}\,\text{viii}$ central optical depth τ_0 , rest-frame equivalent width W_r) of $\text{Ne}\,\text{viii}$ absorption features as a function of the density and the temperature of the absorbing gas. The fundamental assumptions underlying our analytic model are that the gas phase producing $\text{Ne}\,\text{viii}$ absorption: 1) is exposed only to the extragalactic UV background; 2) is in ionisation equilibrium; 3) is embedded within a larger gaseous structure in (quasi) local hydrostatic equilibrium; 4) has an inhomogeneous metal distribution, with the metals filling only a fraction c_L of the volume projected along the sightline across the structure. We present and discuss these two approaches in Sections 2.1 and 2.2, respectively.

The combined results from our simulation and our analytic model –which we discuss in Section 3–, allow us to determine the gas phases in the low redshift Universe that are expected to contain significant amounts of $\text{Ne}\,\text{viii}$ (in term of mass), and to identify these gas phases through their $\text{Ne}\,\text{viii}$ absorption. Our ultimate goal is to aid the interpretation of current observational data (discussed in Section 4), and to provide a guide for future observations aiming to detect $\text{Ne}\,\text{viii}$ absorbing gas using absorption spectroscopy.

We refer the impatient reader to Section 5, where we summarise the central results of our study. A detailed presentation of the status of current $\text{Ne}\,\text{viii}$ detections at low redshift and other results that might be of interest only to the more specialised reader are left for the appendix.

2 LOW-REDSHIFT $\text{Ne}\,\text{viii}$ ABSORBING GAS: SIMULATION AND ANALYTIC MODEL

Seven-times ionised neon ($\text{Ne}\,\text{viii}$) can be produced by the ionisation of $\text{Ne}\,\text{vii}$ (ionisation potential $E_p = 207.271 \pm 0.013 \text{ eV}$; e.g. Kramida & Buchet-Poulizac 2006) via the absorption of photons with energies $E_\gamma \geq E_p$ and by collisions with electrons and other atoms. The $\text{Ne}\,\text{viii}$ ion fraction $f_{\text{Ne}\,\text{viii}} \equiv (n_{\text{Ne}\,\text{viii}}/n_{\text{Ne}})$ produced by both photo-ionisation and collisional ionisation in gas as a function of the gas density and temperature is presented in Figure 1, which we obtain from the tables provided by Wiersma et al. (2009a). These tables, which were also used to calculate the ionisation balance in our simulation (see Section 2.1), were computed with the photoion-

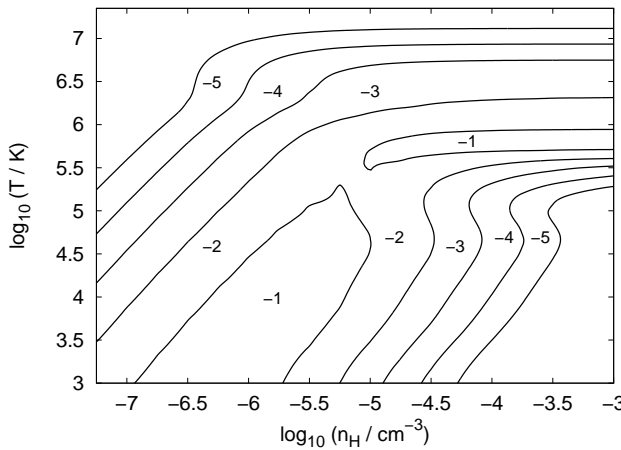


Figure 1. Ne VIII ionisation fraction, $f_{\text{Ne VIII}} \equiv (n_{\text{Ne VIII}}/n_{\text{Ne}})$, of optically thin gas in ionisation equilibrium exposed to the X-Ray/UV background radiation from galaxies and quasars at $z = 0.5$. The numbers in the panel indicate the minimum $f_{\text{Ne VIII}}$ (in logarithmic scale) in gas at the densities and temperatures within the corresponding contour. Note that relatively high ionisation fractions $f_{\text{Ne VIII}} \sim 0.1$ occur in both low-density, low-temperature (photo-ionised) gas with $n_{\text{H}} < 10^{-5} \text{ cm}^{-3}$ and $T < 10^5 \text{ K}$, and in denser, warm-hot (collisionally ionised) gas with $n_{\text{H}} > 10^{-5} \text{ cm}^{-3}$ and $T \approx 5 \times 10^5 \text{ K}$.

isation package CLOUDY (version 07.02.00 of the code last described by Ferland et al. 1998) assuming the gas is exposed to the $z = 0.5$ Haardt & Madau (2001) model for the X-Ray/UV background radiation from quasars and galaxies (assuming a 10 per cent escape fraction for H-ionising photons). In addition, the gas is assumed to be dust-free, optically thin and in ionisation equilibrium. The most striking feature visible in Figure 1 is the high Ne VIII ion fractions, $f_{\text{Ne VIII}} \sim 0.1$, both in photo-ionised gas with $n_{\text{H}} < 10^{-5} \text{ cm}^{-3}$ and $T < 10^5 \text{ K}$, and in collisionally ionised gas with $n_{\text{H}} > 10^{-5} \text{ cm}^{-3}$ and $T \approx 5 \times 10^5 \text{ K}$. This is remarkable because it indicates that the presence of measurable Ne VIII absorption in spectra may by itself not be a sufficient condition for the detection of gas at $T > 10^5 \text{ K}$.

It is therefore important to explore in detail the connection between the physical conditions of the gas harbouring Ne VIII and the characteristics of the Ne VIII absorption it produces, which we do next using numerical simulations and analytic methods.

2.1 Simulation

The simulation used in this work is one of the several cosmological simulations that together comprise the OverWhelmingly Large Simulations (OWLS) project, described in detail in Schaye et al. (2010). These simulations were performed with a significantly extended version of the *N*-Body, Tree-PM, Smoothed Particle Hydrodynamics (SPH) code GADGET III – which is a modified version of GADGET II (last described in Springel 2005) –, a Lagrangian code used to calculate gravitational and hydrodynamic forces on a system of particles.

Here we focus on a particular model from the OWLS suite referred to as *AGN*. This model adopts a flat Λ CDM cosmology characterised by the set of parameters $\{\Omega_m, \Omega_b, \Omega_\Lambda, \sigma_8, n_s, h\} = \{0.238, 0.0418, 0.762, 0.74, 0.95, 0.73\}$ as derived from the Wilkinson Microwave Anisotropy Probe (WMAP) 3-year data² (Spergel

² These parameter values are largely consistent with the WMAP 7-year

et al. 2007). This model includes star formation following Schaye & Dalla Vecchia (2008), metal production and timed release of mass and heavy elements by intermediate mass stars, i.e., asymptotic giant-branch (AGB) stars and supernovae of Type Ia (SNIa), and by massive stars (core-collapse supernovae, SNIIf) as described by Wiersma et al. (2009b). It further incorporates kinetic feedback by SNIIf based on the method of Dalla Vecchia & Schaye (2008), as well as thermal feedback by SNIa (Wiersma et al. 2009b). Radiative cooling by hydrogen, helium and heavy elements is included element by element following the method of Wiersma et al. (2009a). The ionisation balance for each SPH particle is computed as a function of redshift, density, and temperature using pre-computed tables obtained with the photoionisation package CLOUDY (version 07.02.00 of the code last described by Ferland et al. 1998), assuming the gas is exposed to the Haardt & Madau (2001) model for the X-Ray/UV background radiation from galaxies and quasars. Additionally, our simulation includes feedback by active galactic nuclei (AGN) based on the model of black hole growth developed by Booth & Schaye (2009), which is a modified version of the model by Springel et al. (2005). Our simulation was run in a cubic box of $100h^{-1}$ comoving mega-parsec (Mpc) on a side, containing 512^3 dark matter (DM) particles and equally many baryonic particles. The initial particle mass is $4.1 \times 10^8 h^{-1} M_\odot$ (DM) and $8.7 \times 10^7 h^{-1} M_\odot$ (baryonic). The gravitational softening is set to $8 h^{-1}$ comoving kilo-parsec (kpc) and is fixed at $2h^{-1}$ proper kpc below $z = 3$.

It is worth noting that this model has been shown to self-consistently reproduce several fundamental measurements, namely: the observed mass density in black holes at $z = 0$; the black hole scaling relations (Booth & Schaye 2009) and their evolution (Booth & Schaye 2011); the observed optical and X-ray properties, stellar-mass fractions, star-formation rates (SFRs), stellar-age distributions and the thermodynamic profiles of groups of galaxies (McCarthy et al. 2010); and the standard H I observables (distribution of H I column densities $N_{\text{H I}}$, distribution of Doppler parameters $b_{\text{H I}}$, $b_{\text{H I}} - N_{\text{H I}}$ correlation) and the BLA line number density at low redshift (Tepper-García et al. 2012). For a more detailed description of this (and other) models that are part of the OWLS project, see Schaye et al. (2010).

2.1.1 Physical conditions of Ne VIII absorbing gas

We investigate the physical state of the gas containing Ne VIII in our simulation at $z = 0.5$ in two different ways. Our first method is to compute the distribution of Ne VIII mass in gas as a function of density and temperature using the density, temperature, and Ne VIII mass of each SPH particle. For the second method we draw a number (5000) of random sightlines through our simulation box and generate and fit a corresponding set of high-S/N, COS-like spectra, using the procedure described in Appendix B. In this way we obtain a sample of roughly 8670 Ne VIII absorption components and we assign each a characteristic (i.e. Ne VIII optical depth weighted) density (n_{H}) and a characteristic temperature (T). To assign a Ne VIII optical depth weighted density (temperature) to an absorber, we follow the procedure described in Tepper-García et al. (2011, their Section 5.1). Briefly, we use our synthetic spectra to compute the density (temperature) weighted by the Ne VIII optical depth in redshift space along the sightline as in Schaye et al. (1999). We then identify

results (Jarosik et al. 2011), the largest difference being the value of σ_8 , which is 2σ lower in the WMAP 3-year data than allowed by the WMAP 7-year data.

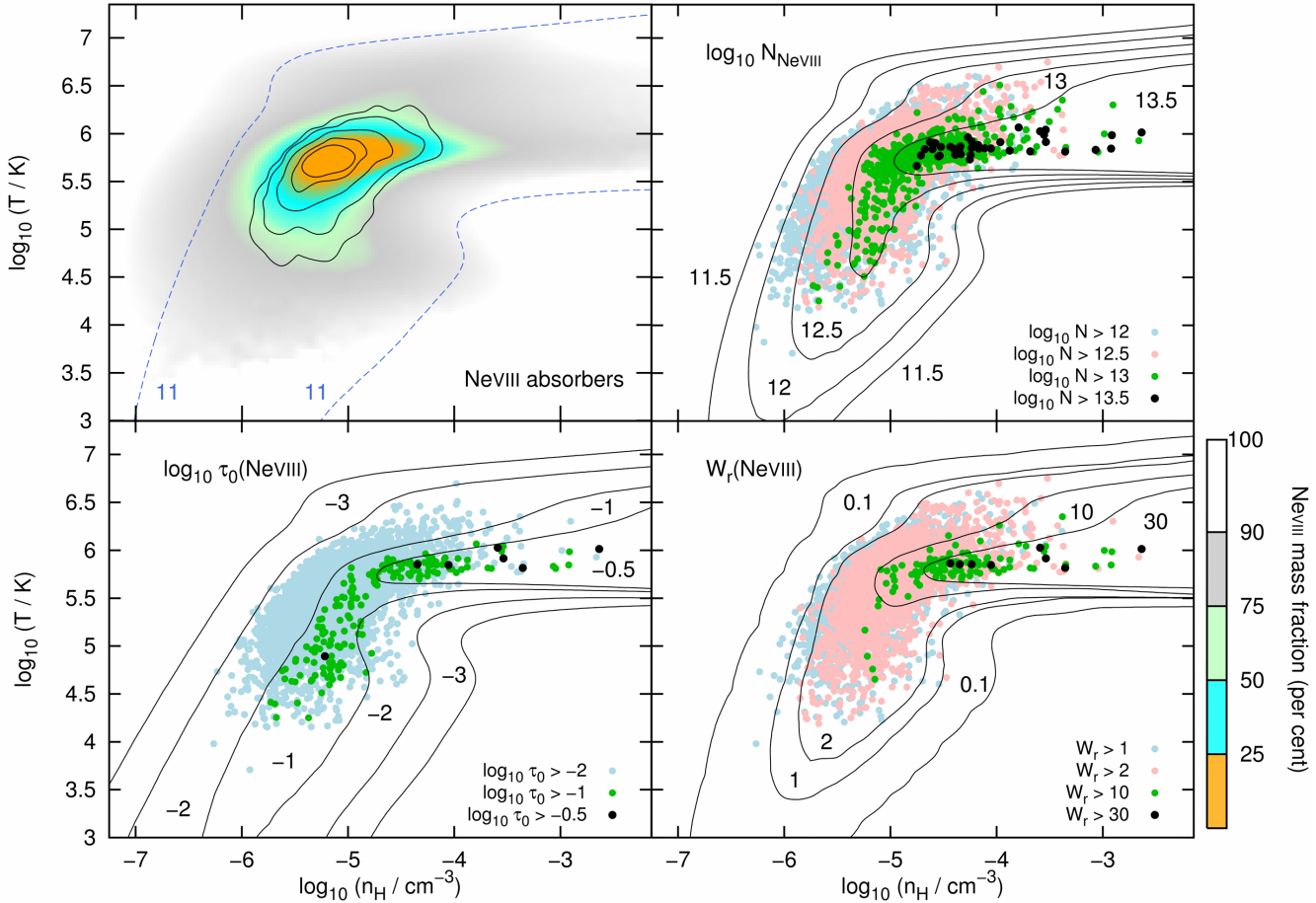


Figure 2. *Top-left:* Distribution of Ne VIII mass in gas in our simulation at $z = 0.5$. The coloured regions show the fraction of Ne VIII mass in gas contained within the corresponding region of $n_{\text{H}} - T$ space, as indicated by the colour bar in the bottom right margin. The solid contours show the distribution (by number) of gas densities and temperatures of the Ne VIII absorbers detected in a set of synthetic spectra at $z = 0.5$; the outer-most contour contains 90 per cent of the absorbers. The blue dashed curves indicate the minimum column density $\log_{10}(N_{\text{Ne VIII}}/\text{cm}^{-2}) = 11$ allowed in our fitting procedure. Note that virtually all the Ne VIII mass in gas and all the detected Ne VIII absorbers are contained within the region defined by this limit. *Top-right:* Scatter plot of Ne VIII absorbers colour-coded by their Ne VIII column density. The solid contours indicate the Ne VIII column density (in cm^{-2}) predicted by our analytic model, equation (7), adopting $[\text{Ne}/\text{H}] = -0.7$ (relative to $\log_{10}(n_{\text{Ne}}/n_{\text{H}})_{\odot} = -3.91$), $f_g = 0.168$ and a filling fraction $\log_{10} c_L = -0.5$. *Bottom-left:* Scatter plot of Ne VIII absorbers colour-coded by their central optical depth. The contours show the Ne VIII central optical depth predicted by our analytic model, equation (10); the values for $[\text{Ne}/\text{H}]$, f_g and c_L are identical to the values adopted before. *Bottom-right:* Scatter plot of Ne VIII absorbers colour-coded by their rest-frame equivalent width (in $\text{m}\text{\AA}$). The contours indicate the Ne VIII rest-frame equivalent width in $\text{m}\text{\AA}$ computed from the Ne VIII column density predicted by our analytic model, equation (11). Note that the Ne VIII gas mass distribution in the top-left panel, and the contours in each panel are identical to the corresponding contours shown in Figure 8. The contours agree with the coloured points, indicating that our analytic model reproduces the simulation results very well.

the pixel corresponding to the absorption line's centre, smooth (i.e. average) over ± 2 pixels around this pixel, and assign this last optical depth weighted average density (temperature) to the absorber. Note that our synthetic spectra have a constant pixel size $\delta v = 3 \text{ km s}^{-1}$, which corresponds to a physical linear path $\delta l \approx 33 \text{ kpc}$ at $z = 0.5$, assuming that the velocity spread is due solely to the Hubble expansion (note that our spectra are computed taking into account also peculiar velocities and thermal broadening). We thus smooth over a range $\Delta v = 12 \text{ km s}^{-1}$ or 132 kpc around the line centre.

The distributions of densities (n_{H}) and temperatures (T) of the Ne VIII gas in our simulation at $z = 0.5$ obtained from these two different approaches are compared in the top-left panel of Figure 2 (note that the other panels will be discussed in Section 2.2). The distribution of Ne VIII mass as a function of n_{H} and T obtained from the density, the temperature, and the Ne VIII mass of each SPH particle is shown by the coloured areas. Each of these is colour coded by the

fraction of Ne VIII mass in gas contained within the corresponding region of $n_{\text{H}} - T$ space, according to the colour bar displayed in the bottom right margin. So, for example, the innermost region (orange) contains 25 per cent of the Ne VIII mass in the simulation; the cyan and the orange area together enclose 50 per cent of the Ne VIII mass, and so on. The black contours show the distribution of Ne VIII optical depth weighted densities and temperatures of the Ne VIII absorbers detected in our simulated spectra. These contours enclose, starting from the innermost, 20, 40, 60, 80, and 90 per cent of the total number of absorbers. Note that the physical conditions of the Ne VIII absorbing gas inferred from the spectra (black contours) match the corresponding intrinsic properties of the Ne VIII harbouring gas in the simulation (coloured regions) very well. This confirms that our choice of assigning physical quantities to the absorbers identified in synthetic spectra by using optical depth weighted quantities is a

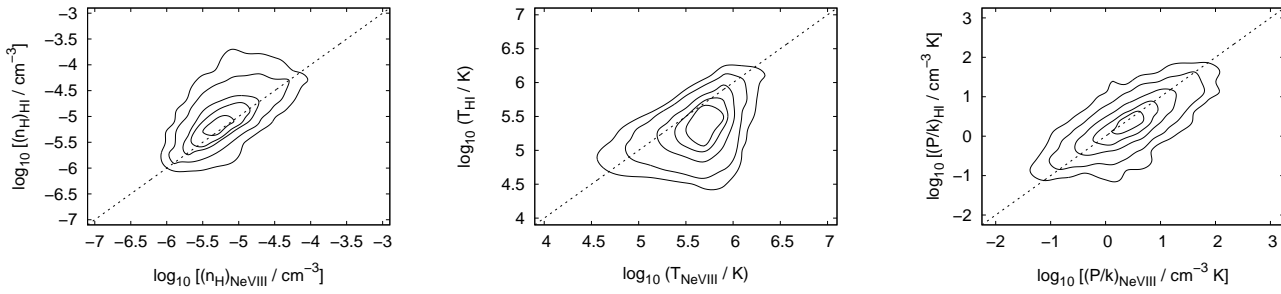


Figure 3. Comparison of the density (left), temperature (centre), and thermal pressure (right) of the Ne VIII absorbing gas and that of the gas responsible for the H I absorption at the same location in redshift space.

reliable method to unequivocally link the absorption of the gas to its physical state.

We find that most of the Ne VIII mass in our simulation resides in gas with densities with densities $10^{-6} \lesssim (n_{\text{H}}/\text{cm}^{-3}) \lesssim 10^{-4}$ (or roughly 1 – 150 times the cosmic mean at $z = 0.5$) and temperatures $10^5 \lesssim (T/\text{K}) \lesssim 10^6$. Hence, even though the Ne VIII ion fraction can be high both in photo- and collisionally ionised gas (see Figure 1), our simulation predicts that most of the Ne VIII is produced by collisional ionisation in low-density gas in ionisation equilibrium. This result disagrees in part with Oppenheimer et al. (2012), who find that most of the Ne VIII mass in their simulation (albeit at $z = 1$) is also in gas with densities $n_{\text{H}} \sim 10^{-5}\text{cm}^{-3}$, but at significantly lower temperatures, only slightly above $T \sim 10^4\text{ K}$. We note that we do find in our simulation Ne VIII absorbers with $T < 10^5\text{ K}$ (see scatter plots in Figure 2); however, these are generally weak and their relative number is low.

A similar discrepancy concerning the typical temperature of O VI absorbing gas between Oppenheimer et al.’s simulations and ours was reported in Tepper-García et al. (2011). Oppenheimer et al. attribute the low fraction of highly-ionised metal absorbers with $T \gtrsim 10^5\text{ K}$ in their simulation to the fact that their simulation does not resolve conductive interfaces within halos. Since our simulation does not resolve such interfaces either, the difference in the predicted temperature distribution of Ne VIII (or O VI) absorbing gas most probably stems from the difference in the implementations of the sub-grid physics; in particular, the prescription to model winds on galactic scales may be crucial since these determine the distribution of mass and heavy elements among the different gas phases. Also, the assumption of ionisation equilibrium, which is also used by Oppenheimer et al. (2012), may be important (e.g. Oppenheimer & Schaye 2013b,a) and future studies relaxing this assumption may obtain different results. We therefore advise that the physical conditions, in particular the thermal state, of highly ionised gas predicted by simulations should be taken with caution.

As will be explained in more detail in Section 2.2, two of the implicit assumptions underlying our analytic model are that the density (n_{H}) and the temperature (T) of the Ne VIII absorbing clouds are comparable to the local density and the local temperature of the surrounding gas. This is reflected in the fact that the Ne VIII column density (and all the other derived spectral properties) as given by equation (7) depends on $n_{\text{H}}L_J$, where L_J itself depends on n_{H} and T (see equation 4). Moreover, since $n_{\text{H}}L_J \propto (n_{\text{H}}T)^{1/2} = (P/k)^{1/2}$ (where P is the thermal pressure and k is Boltzmann’s constant), these assumptions imply that the metal absorbers are not far from thermal pressure equilibrium with their surrounding (i.e. confining) medium.

In order to investigate if these conditions are satisfied by the

Ne VIII absorbing gas in our simulation, we compare the characteristic density (n_{H}), temperature (T), and thermal pressure ($P/k \equiv n_{\text{H}}T$) of each Ne VIII absorber in our sample with the corresponding quantity of the associated (i.e. aligned in velocity space) H I absorber. To this end, we compute the Ne VIII- and the H I-optical depth weighted density and temperature at the centre of each Ne VIII absorbing component identified in our simulated spectra, following the previously described procedure. Note that when comparing H I to Ne VIII weighted quantities, it is implicitly assumed that relative peculiar velocities between the Ne VIII and H I absorbing phases are small, so that their alignment in velocity space implies their coincidence in physical space. The comparison of the densities, temperatures, and the thermal pressures thus obtained is shown in Figure 3. In each panel, the x -axis indicates the physical quantity (e.g. density) weighted by the Ne VIII optical depth and the y -axis indicates the corresponding quantity weighted by the H I optical depth. The contours lines show the distribution (by number) of absorbers; these contours enclose, starting from the innermost, 20, 40, 60, 80, and 90 per cent of the total number of absorbers. The dotted line along the diagonal indicates in each case a perfect match between the two physical quantities considered.

The left panel of Figure 3 shows that the density of the Ne VIII absorbing gas is similar to the density of the surrounding gas for most of the Ne VIII absorbers, being only slightly higher on average in the H I absorbing phase with $n_{\text{H}} \gtrsim 10^{-5}\text{cm}^{-3}$. In the middle panel we see that, while the temperature of both these phases is comparable for most of the absorbers, for a non-negligible fraction of the absorbers it is a factor ~ 10 higher in the Ne VIII absorbing phase than in the H I absorbing phase. The right panel demonstrates that the thermal pressure (P/k) is very similar in both gas phases; in other words, the phases are, on average, in pressure equilibrium with each other. These results suggest that a typical Ne VIII absorber corresponds to a metal-enriched pocket of warm-hot gas confined by a slightly denser and cooler gaseous structure.

2.1.2 Absorption line statistics

Using the sample of Ne VIII absorption components obtained from our set of synthetic spectra (see Section 2.1 and Appendix B), we compute the Ne VIII line number density and the distribution of Ne VIII column densities at $z = 0.5$. The results are shown in Figures 5 and 6, respectively, and discussed below. An example of a strong Ne VIII absorption feature produced in gas with $\log_{10}(n_{\text{H}}/\text{cm}^{-3}) \approx -3.5$ and $\log_{10}(T/\text{K}) \approx 6.1$ along a random sightline in our simulation at $z = 0.5$ and its decomposition into

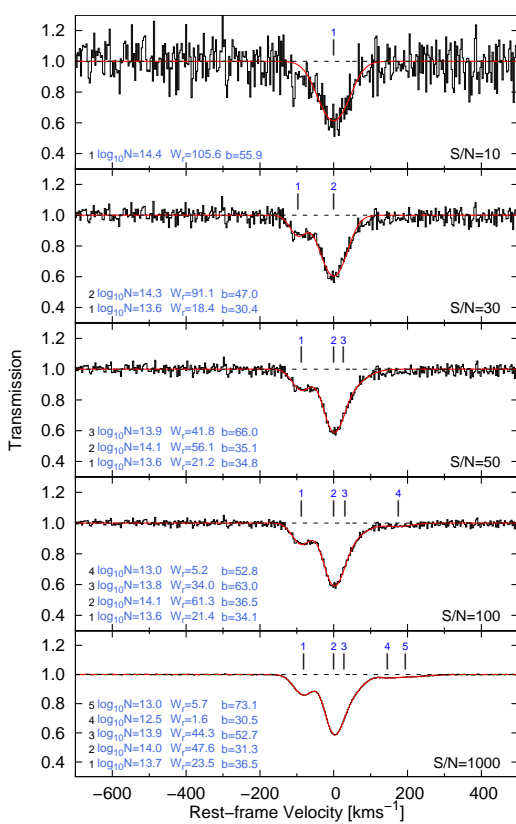


Figure 4. Ne VIII absorption feature with total $\log_{10}(N_{\text{Ne VIII}}/\text{cm}^{-2}) \approx 14.4$ along a random sightline drawn from our simulation at $z = 0.5$ in a synthetic COS-like spectrum adopting different S/N values (black histogram) and the corresponding fits (red). The vertical dashes mark the velocity centre of each fitted component; their corresponding logarithmic column density, rest-frame equivalent width (in mÅ), and Doppler parameter (in km s^{-1}) are listed in the bottom-left of each panel. While the equivalent width (W_r) and column density ($N_{\text{Ne VIII}}$) integrated across the absorber are roughly the same for different S/N values ($W_r \approx 105 \text{ m}\text{\AA}$ and $\log_{10}(N_{\text{Ne VIII}}/\text{cm}^{-2}) \approx 14.4$, respectively), the values of W_r and $N_{\text{Ne VIII}}$ of the individual components vary substantially from panel to panel since a different number of components is required in each case to produce a good fit. Note that all fits have a reduced $\chi^2 \sim 1$ (see Appendix B for details on the fitting procedure). This peculiar absorption feature is produced in gas with $\log_{10}(n_{\text{H}}/\text{cm}^{-3}) \approx -3.5$ and $\log_{10}(T/\text{K}) \approx 6.1$.

individual Gaussian components is shown in Figure 4 (see the figure caption for more details).

Figure 5 displays the number of Ne VIII absorption components per unit redshift with rest-frame equivalent width above a given threshold, $dN/dz(W > W_r)$, predicted by our simulation at $z = 0.5$ (black) and the corresponding Poisson uncertainty (gray shaded area). The blue dashed curve shows the probability distribution (indicated by the right y -axis) of rest-frame equivalent widths, which has a median value $W_r = 1.23 \text{ m}\text{\AA}$ (indicated by the vertical dashed line). Thus, roughly half of the Ne VIII absorbers in our high-S/N (i.e. S/N=1000) simulated spectra have $W_r \lesssim 1 \text{ m}\text{\AA}$, while the other half have a rest-frame equivalent width in the range $1 \text{ m}\text{\AA} < W_r \lesssim 10 \text{ m}\text{\AA}$, with a very small fraction having $W_r \gtrsim 10 \text{ m}\text{\AA}$, $dN/dz(W > 10 \text{ m}\text{\AA}) \sim 1$, and an even smaller fraction with $W_r > 30 \text{ m}\text{\AA}$, $dN/dz(W > 30 \text{ m}\text{\AA}) \sim 10^{-1}$.

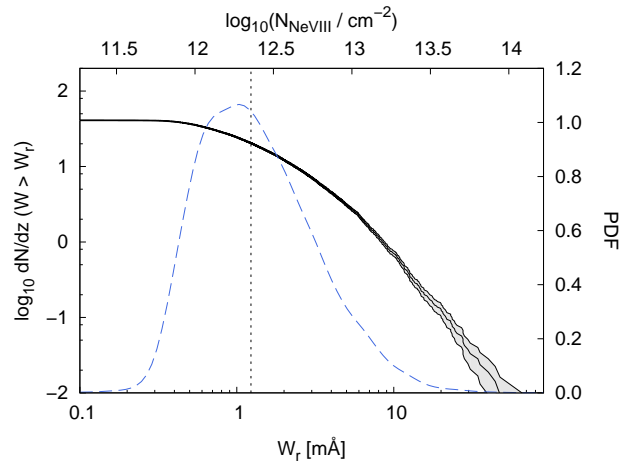


Figure 5. Number of Ne VIII absorption components per unit redshift above a given rest-frame equivalent width ($dN/dz(W > W_r)$; black curve) and the corresponding Poisson uncertainty (shaded area) obtained from a set of simulated COS-like spectra with $S/N=1000$ along 5000 random sightlines drawn from our simulation at $z = 0.5$. The top x -axis indicates the approximate Ne VIII column density corresponding to a given rest-frame equivalent width. The blue dashed curve shows the probability distribution of Ne VIII equivalent widths; its amplitude is indicated by the y -axis on the right. The vertical dotted line indicates the median value $W_r = 1.23 \text{ m}\text{\AA}$. Note the small fraction of absorbers with $W_r > 10 \text{ m}\text{\AA}$.

The value of the cumulative line frequency for $W_r > 30 \text{ m}\text{\AA}$ we find is consistent with the predictions from other simulations (Oppenheimer et al. 2012), but significantly lower than the values obtained from current observations. Narayanan et al. (2009) give $dN/dz(W > 30 \text{ m}\text{\AA}) = 2.1$ (no error quoted), which they estimate indirectly from the O VI line-number density at comparable redshifts, assuming every seventh O VI absorber has associated Ne VIII absorption. Based on three detections along a single sightline, Meiring et al. (2012) obtain $dN/dz(W > 30 \text{ m}\text{\AA}) = 7_{-3}^{+7}$, which is only consistent with the value given by Narayanan et al. (2009) at the lower 2σ level. The poor agreement between these two measurements stems most probably from the fact that they rely on very few detections along small total redshift paths, and they are therefore highly uncertain. In particular, it is possible that the measured line frequencies have been overestimated. Increasing the sensitivity of the data would reveal weaker Ne VIII absorbers along many more sightlines, thus increasing the number of detections but also the surveyed redshift path. It is, however, not clear whether the measured line frequency would converge to a value which is more in line with the result from our simulation. Alternatively, we consider the possibility that the low rate of Ne VIII absorbers with $W_r \gtrsim 30 \text{ m}\text{\AA}$ (or $\log_{10}(N_{\text{Ne VIII}}/\text{cm}^{-2}) \gtrsim 14$) in our simulation might be an artefact related to the lack of high equivalent width O VI absorbers in our (Tepper-García et al. 2011) and other (e.g. Oppenheimer & Davé 2009) simulations that may result from turbulent mechanisms on sub-resolution scales which are not properly captured by these simulations. It is also possible that the observed strong Ne VIII (and O VI) absorbers trace fossil AGN proximity zones (Oppenheimer & Schaye 2013a). Ultimately, however, a significantly larger volume of data is required to get a reliable estimate of $dN/dz(W > W_r)$, and to test our predicted value of $dN/dz(W > 30 \text{ m}\text{\AA}) \sim 10^{-1}$.

Figure 6 shows the distribution of Ne VIII column densit-

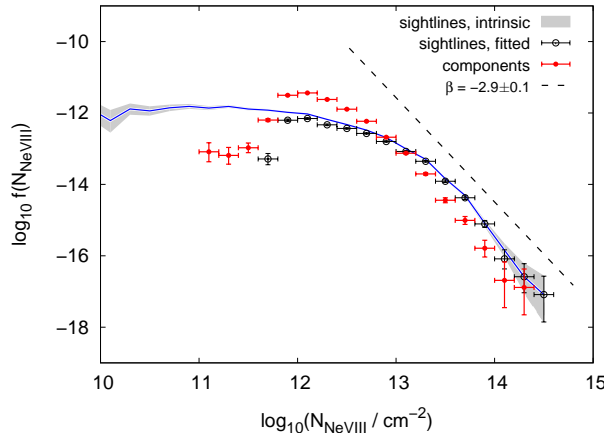


Figure 6. Distribution of Ne VIII column densities per unit $N_{\text{Ne VIII}}$ per unit absorption distance, $f(N_{\text{Ne VIII}}) \equiv \partial^2 N / \partial \chi \partial N_{\text{Ne VIII}}$ of the components identified in a set of simulated high-S/N, COS-like spectra along 5000 random sightlines drawn from our simulation at $z = 0.5$ (red symbols). The black symbols show the distribution of column densities integrated (i.e. adding up all the fitted components) along each spectrum; the blue curve show the distribution of *intrinsic* column densities integrated along each corresponding physical sightline; the error bars along the y -axis and the shaded area indicate the corresponding Poisson scatter. The dashed line shows a fit to the red symbols in the range $\log_{10}(N_{\text{Ne VIII}}/\text{cm}^{-2}) \in [12.5, 14.5]$ in the form of a power-law with slope $\beta = -2.9 \pm 0.1$. Note that the line has been shifted upwards for display purposes.

ies per unit $N_{\text{Ne VIII}}$ per unit absorption distance,³ $f(N_{\text{Ne VIII}}) \equiv \partial^2 N / \partial \chi \partial N_{\text{Ne VIII}}$, in our simulation at $z = 0.5$. The red symbols show the distribution of Ne VIII column densities (CDDF) of the components identified in a set of high-S/N, COS-like spectra along 5000 random sightlines. The dashed line corresponds to the fit in the form of a power-law with slope $\beta = -2.9 \pm 0.1$ to the red symbols in the range $\log_{10}(N_{\text{Ne VIII}}/\text{cm}^{-2}) \in [12.5, 14.5]$, and it has been shifted upwards for display purposes. We note that the slope $\beta = -2.9 \pm 0.1$ of the Ne VIII CDDF at $z = 0.5$ is significantly steeper⁴ than the slope $\beta = -2.1 \pm 0.1$ of the O VI CDDF obtained from observations (Tilton et al. 2012) and found in our simulations at a somewhat lower redshift ($z = 0.25$; Tepper-García et al. 2011).

The black symbols in Figure 6 show the distribution of column densities integrated (i.e. adding up the column densities of all identified components) along each spectrum of size 8340 km s^{-1} at $z = 0.5$. The error bars along the y -axis indicate the corresponding Poisson uncertainty. The blue curve and the shaded area show the distribution of *intrinsic* Ne VIII column densities integrated along each corresponding physical sightline of length $100h^{-1} \text{ Mpc}$ (comoving) and its Poisson uncertainty, respectively. A perfect match between

³ The absorption distance in a flat Universe dominated by matter and Dark Energy is given by

$$d\chi = (1+z)^2 [\Omega_m(1+z)^3 + \Omega_\Lambda]^{-1/2} dz.$$

⁴ The slope found by Tilton et al. (2012) and Tepper-García et al. (2011) is obtained from the analysis of observed and simulated spectra, respectively, with moderate S/N: 10 – 30. Using the set of high-S/N, COS-like synthetic spectra of this study, we find $\beta = -2.0 \pm 0.1$ for the O VI CDDF, which is consistent with the slope obtained in our previous work from simulated spectra with S/N = 10 – 30.

the black and the blue distributions would indicate that the totality of the Ne VIII (mass) is detected in absorption. The recovery is excellent for $N_{\text{Ne VIII}} > 10^{12} \text{ cm}^{-2}$. However, while the distribution of integrated, *intrinsic* column densities (blue / shaded) flattens off at column densities $N_{\text{Ne VIII}} \sim 10^{12} \text{ cm}^{-2}$, the distribution of column densities measured from the spectra (black / red) drops sharply⁵ at $N_{\text{Ne VIII}} \lesssim 10^{12} \text{ cm}^{-2}$. Thus, Ne VIII absorbers with $N_{\text{Ne VIII}} \lesssim 10^{12} \text{ cm}^{-2}$ should exist but their detection in absorption spectra requires $S/N > 1000$. From the baryon content in the form of Ne VIII in the simulation, $\Omega_{\text{Ne VIII}}^{\text{sim}} = 2.70 \times 10^{-8}$, and the baryon content in the form of Ne VIII recovered from the spectra, $\Omega_{\text{Ne VIII}}^{\text{fit}} = 2.25 \times 10^{-8}$, we estimate that the fraction of Ne VIII mass in absorbers with $N_{\text{Ne VIII}} < 10^{12} \text{ cm}^{-2}$ is roughly 20 per cent.

2.2 Analytic model

Now that we have discussed the physical conditions of the gas containing Ne VIII in our simulation, we proceed to investigate the connection between the physical state and the absorption signatures of this gas phase using an independent approach. As we have done in Tepper-García et al. (2012) for H I, our goal here is to develop a model that allows us to predict the Ne VIII line observables (column density, equivalent width, central optical depth), and the spectral sensitivity in terms of S/N required to detect Ne VIII absorbing gas as a function of the gas density (n_{H}) and the gas temperature (T). Conversely, such a model should allow one to constrain the physical state of the absorbing gas from its observed absorption characteristics.

The Ne VIII central optical depth of an absorption line with column density $N_{\text{Ne VIII}}$ and Doppler parameter $b_{\text{Ne VIII}}$ is given by

$$\begin{aligned} \tau_0(\text{Ne VIII}) &= \sqrt{\pi} r_e c \lambda_0 f_0 \left(\frac{N_{\text{Ne VIII}}}{b_{\text{Ne VIII}}} \right) \\ &\approx 0.596 \left(\frac{N_{\text{Ne VIII}}}{10^{14} \text{ cm}^{-2}} \right) \left(\frac{b_{\text{Ne VIII}}}{20 \text{ km s}^{-1}} \right)^{-1}, \end{aligned} \quad (1)$$

where $r_e = 2.82 \times 10^{-13} \text{ cm}$ is the classical electron radius (Mohr et al. 2012), $c \approx 3.00 \times 10^{10} \text{ cm s}^{-1}$ is the speed of light in vacuum, and λ_0 and f_0 are the transition's rest wavelength and oscillator strength, respectively; the coefficient in the equation above is obtained for the Ne VIII $\lambda_0 = 770.41 \text{ \AA}$ transition with $f_0 = 0.103$ (Verner et al. 1994).

Since τ_0 , the equivalent width and the sensitivity in terms of S/N all depend on $N_{\text{Ne VIII}}$ and $b_{\text{Ne VIII}}$ (see equations 11 and 12 below), our problem reduces to finding expressions for these two quantities in terms of n_{H} and T . As a starting point, we assume that the Ne VIII column density can be computed as

$$N_{\text{Ne VIII}} = \int_0^l n_{\text{Ne VIII}} dl'. \quad (2)$$

Here, l is the physical, linear extension of the gaseous, Ne VIII absorbing structure (or ‘cloudlet’), and $n_{\text{Ne VIII}}$ is the corresponding Ne VIII particle density, which can be expressed in terms of the Ne VIII ion fraction, $f_{\text{Ne VIII}} \equiv (n_{\text{Ne VIII}}/n_{\text{Ne}})$, and the neon abundance (by number)

⁵ The fact that the Ne VIII detection limit in our synthetic spectra with S/N=1000 and the flattening of the Ne VIII CDDF both correspond to $N_{\text{Ne VIII}} \sim 10^{12} \text{ cm}^{-2}$ is only coincidental and has therefore no deeper meaning.

relative to hydrogen, $(n_{\text{Ne}}/n_{\text{H}})$, as

$$n_{\text{Ne VIII}} = \left(\frac{n_{\text{Ne VIII}}}{n_{\text{Ne}}} \right) \left(\frac{n_{\text{Ne}}}{n_{\text{H}}} \right) n_{\text{H}} = f_{\text{Ne VIII}} \left(\frac{n_{\text{Ne}}}{n_{\text{H}}} \right) n_{\text{H}}. \quad (3)$$

Let us now assume that the absorbing structures are self-gravitating and therefore typically have linear sizes on the order of the local Jeans length (Schaye 2001)

$$L_J = 0.169 \text{ Mpc} (n_{\text{H}}/10^{-5} \text{ cm}^{-3})^{-1/2} \times (T/10^4 \text{ K})^{1/2} (f_g/0.168)^{1/2}, \quad (4)$$

where, f_g is the gas mass fraction and $f_g \equiv \Omega_b/\Omega_m = 0.168$ its universal value.⁶

While equation (4) is reasonable,⁷ we need to take into account that the distribution of intergalactic metals is rather inhomogeneous⁸ on scales $\lesssim 10^2$ kpc (Schaye et al. 2003) and even on scales $\lesssim 1$ kpc (Schaye et al. 2007). We do this by introducing a factor, c_L , which gives the average filling fraction of the metal cloudlets along the gas cloud, in such a way that the total intersected metal absorbing path length (or the integrated linear size of the metal absorber) is

$$l = c_L L_J. \quad (5)$$

Note that, by definition, $0 < c_L \leq 1$, where $c_L \ll 1$ implies a very inhomogeneous, and $c_L \approx 1$ a very homogeneous metal distribution across the gas structure.

If the physical conditions (i.e. temperature, density), the ionisation state and the neon abundance across the metal absorber are uniform, then equation (2) simplifies to

$$N_{\text{Ne VIII}} = f_{\text{Ne VIII}} \left(\frac{n_{\text{Ne}}}{n_{\text{H}}} \right) c_L L_J n_{\text{H}}. \quad (6)$$

Plugging equation (4) into the above equation yields

$$N_{\text{Ne VIII}} = 5.90 \times 10^{14} \text{ cm}^{-2} c_L 10^{[\text{Ne/H}]} \left(\frac{f_{\text{Ne VIII}}}{0.130} \right) \times \left(\frac{n_{\text{H}}}{10^{-5} \text{ cm}^{-3}} \right)^{1/2} \left(\frac{T}{5 \times 10^5 \text{ K}} \right)^{1/2} \left(\frac{f_g}{0.168} \right)^{1/2}. \quad (7)$$

where $[\text{Ne/H}] \equiv \log_{10} (n_{\text{Ne}}/n_{\text{H}}) - \log_{10} (n_{\text{Ne}}/n_{\text{H}})_\odot$. The fiducial values we have inserted in the above equation correspond to the peak ionisation fraction of Ne VIII in CIE, $f_{\text{Ne VIII}} = 0.130$ (Sutherland & Dopita 1993), the (approximate) corresponding peak temperature, $T = 5 \times 10^5 \text{ K}$, and the solar neon abundance $\log_{10} (n_{\text{Ne}}/n_{\text{H}})_\odot = -3.91$ given by Anders & Grevesse (1989, their Table 2). Equation (7) readily shows that the Ne VIII column density of gas with $T \approx 5 \times 10^5 \text{ K}$ and $n_{\text{H}} \sim 10^{-5}$, and a neon abundance $[\text{Ne/H}] = -0.5$ is $N_{\text{Ne VIII}} \sim 10^{14} \text{ cm}^{-2}$, assuming $f_g = 0.168$ and that the metals are homogeneously distributed across the structure, i.e. $c_L \equiv 1$.

In general, both thermal and non-thermal (e.g. turbulence, Hubble expansion) mechanisms will contribute to the total line width. If both types of mechanisms are stochastic and if they both

⁶ The total mass density parameter is $\Omega_m = \Omega_b + \Omega_{\text{DM}}$. The most recent measurements of the baryonic and dark matter density parameters yield, respectively, $\Omega_b = 0.0449 \pm 0.0028$ and $\Omega_{\text{DM}} = 0.222 \pm 0.026$ (Jarosik et al. 2011).

⁷ We have shown (Tepper-García et al. 2012; see also Altay et al. 2011; Rahmati et al. 2012) that our simulation (albeit at $z = 0.25$) is consistent with the assumption that typical H I absorbers are self-gravitating clouds in hydrostatic equilibrium with sizes $\sim L_J$.

⁸ The results by Schaye et al. (2007) correspond to observed metal-line absorbers at $z \approx 2.3$.

obey a Gaussian distribution, then the total line width may be expressed in terms of the thermal (b_T) and non-thermal (b_{nt}) broadening as

$$b_{\text{Ne VIII}}^2 = b_T^2 + b_{nt}^2 = \left(\frac{2kT}{m_{\text{Ne}}} \right) + b_{nt}^2, \quad (8)$$

where Boltzmann's constant $k = 1.38 \times 10^{-16} \text{ erg K}^{-1}$, and $m_{\text{Ne}} = 33.5 \times 10^{-24} \text{ g}$ is the mass of the neon atom (Mohr et al. 2012). The line broadening due to non-thermal processes, in particular turbulent mechanisms, might be difficult to model. However, as we show in Appendix B (see Figure A1), the intrinsic width of the Ne VIII absorption lines in our simulation at $z = 0.5$ is dominated by thermal broadening, i.e. $b_T \gg b_{nt}$, such that the total line width may be well approximated by

$$b_{\text{Ne VIII}} \approx b_T = 20.3 \text{ km s}^{-1} \left(\frac{T}{5 \times 10^5 \text{ K}} \right)^{1/2}. \quad (9)$$

Using equations (1), (7), and (9) we get

$$\tau_0(\text{Ne VIII}) = 3.46 c_L 10^{[\text{Ne/H}]} \left(\frac{f_{\text{Ne VIII}}}{0.130} \right) \times \left(\frac{n_{\text{H}}}{10^{-5} \text{ cm}^{-3}} \right)^{1/2} \left(\frac{f_g}{0.168} \right)^{1/2}. \quad (10)$$

The above equation shows that, even for a density as low as $n_{\text{H}} \sim 10^{-5} \text{ cm}^{-3}$ and a metallicity $[\text{Ne/H}] = -0.5$, the opacity at the line centre of Ne VIII absorbing gas with a temperature close to the peak temperature of the Ne VIII ionisation fraction in CIE ($T \approx 5 \times 10^5 \text{ K}$) is high, $\tau_0 \sim 1$, provided that the metals are well mixed within the absorbing structure ($c_L \approx 1$).

Given a line strength τ_0 , we compute the corresponding rest-frame equivalent width using

$$W_r = \int_{-\infty}^{+\infty} (1 - e^{-\tau(x)}) dx, \quad (11)$$

where $\tau(x) = \tau_0 \exp(-x^2)$, $x \equiv (\lambda - \lambda_0)/\Delta\lambda_D$, and $\Delta\lambda_D = \lambda_0(b_{\text{Ne VIII}}/c)$.

Finally, the sensitivity in terms of the signal-to-noise ratio (S/N) required to detect gas at significance $N\sigma$ and the corresponding line strength are related by

$$N\sigma \sim N(\text{S/N})^{-1} \sim (1 - e^{-\tau_0}) \approx \tau_0, \quad \tau_0 \ll 1. \quad (12)$$

Equations (7), (9), (10), (11), and (12) thus constitute the solution to our problem. Of course, these equations are not restricted to Ne VIII; they can easily be modified to describe the absorption by any ion of any other metal.

In addition to the observables considered above, we provide an estimate of the total hydrogen column density (N_{H}) and the neutral hydrogen column density (N_{H1}) of the Ne VIII cloudlets using

$$N_{\text{H}} \equiv n_{\text{H}} l \quad (13)$$

and

$$N_{\text{H1}} \equiv f_{\text{H1}} N_{\text{H}} \quad (14)$$

where $f_{\text{H1}} \equiv (n_{\text{H1}}/n_{\text{H}})$ is the H I ionisation fraction; this is obtained from the same ionisation model we use to compute the Ne VIII ionisation fraction ($f_{\text{Ne VIII}}$; see Section 2).

The actual observables, however, are the column densities of the gas harbouring the Ne VIII cloudlets, which we denote by $N_{\text{H}}' = n_{\text{H}} L_J$ and $N_{\text{H1}}' = f_{\text{H1}} N_{\text{H}}'$. Note that each of these quantities differs from the corresponding quantity (equations 13 and 14) by a

factor c_L^{-1} , i.e. $N_{\text{H}}' = N_{\text{H}} c_L^{-1}$ and $N_{\text{H}_1}' = N_{\text{H}_1} c_L^{-1}$.

We close this section with an important remark: Strictly speaking, the particle density n_{H} and the temperature T *explicitly* entering equation (6) and equation (9), respectively, correspond to the particle density and to the temperature of the metal cloudlets, whereas the particle density and temperature *implicit* in equation (6; and all derived equations) through $L_J \equiv L_J(n_{\text{H}}, T)$ refer to the particle density and to the temperature of the surrounding gas. These quantities need not be equal, in general. However, in deriving equations (7) and (10) we have implicitly assumed they are (at least) of the same order of magnitude. As we have shown previously in Section 2.1, this assumption is well justified.

2.2.1 Setting the model parameters

Our analytic model depends basically on two parameters: 1) c_L , which measures the homogeneity of the metal distribution within the gas structure; and 2) the (average) neon abundance ($n_{\text{Ne}}/n_{\text{H}}$) in the absorbing gas. The first parameter, c_L , is a free parameter that needs to be calibrated e.g. using simulations. The second parameter, ($n_{\text{Ne}}/n_{\text{H}}$), should be constrained by observations. Ideally, the value of c_L obtained from our simulation should be consistent with observations as well; and likewise, the value of ($n_{\text{Ne}}/n_{\text{H}}$) constrained by observations should be consistent with the typical neon abundance of Ne VIII absorbers in our simulation.

Let us start by considering the second parameter. Figure 7 shows the distribution of the neon abundance, $[\text{Ne}/\text{H}] \equiv \log_{10}(n_{\text{Ne}}/n_{\text{H}}) - \log_{10}(n_{\text{Ne}}/n_{\text{H}})_{\odot}$, in gas in our simulation at $z = 0.5$, adopting $\log_{10}(n_{\text{Ne}}/n_{\text{H}})_{\odot} = -3.91$. The left panel shows the mass-weighted average of the neon abundance in gas as a function of the gas density and temperature. The contours in this panel indicate the distribution of Ne VIII mass in gas, and correspond to the distribution shown in colour in the top-left panel of Figure 2.

The right panel displays the distribution of $[\text{Ne}/\text{H}]$ values in the Ne VIII absorbing gas in our simulation at $z = 0.5$ (blue curve). The full range of neon abundances measured in some of the Ne VIII absorbers observed at low redshift is indicated by the shaded area. The data points in both panels represent a subset of the observed Ne VIII absorbers listed in Table 1. This figure shows that the neon abundance of the Ne VIII absorbers in our simulation is distributed over the range $-1.5 \lesssim [\text{Ne}/\text{H}] \lesssim 0$, with median $[\text{Ne}/\text{H}] = -0.7$. Clearly, the average neon abundance of the gas in our simulation is broadly consistent with the neon abundance of the observed Ne VIII absorbers (data points) at similar densities and temperatures, although our simulation favours slightly lower values. In principle we could tabulate the mass-weighted mean of $(n_{\text{Ne}}/n_{\text{H}})$ obtained from our simulation as a function of n_{H} and T and use it as input in our analytic model. However, for simplicity and as a first approach, we have chosen to fix the neon abundance in our analytic model to the median value $[\text{Ne}/\text{H}] = -0.7$ found in Ne VIII absorbing gas in our simulation. This choice is supported by the fact that the metallicity of the warm-hot gas in our simulations is robust to changes in the sub-grid physics and evolves only slowly (Wiersma et al. 2011).

Next we need to set the value of the parameter c_L . As mentioned before, this is a free parameter whose exact value cannot be set *a priori*. However, it is possible to constrain the range of values beforehand. For instance, by definition a value $c \approx 1$ implies that the metals are homogeneously distributed across the structure; also, by virtue of equations (4), (5), and (7), such a value implies that the sizes of absorbers with $N_{\text{Ne VIII}} \sim 10^{14}$ are on the order of 1 Mpc,

neither of which is consistent with observations (see Section 4). Thus, values in the range $c_L \ll 1$ seem more plausible.

To determine the value of c_L more precisely, we choose the following approach: First, we measure the Ne VIII column density ($N_{\text{Ne VIII}}$), the rest-frame equivalent width (W_r) and the central optical depth (τ_0) for each Ne VIII absorber identified in the synthetic spectra obtained from our simulation, as explained in Appendix B. We use for this purpose the sample of absorbers identified in simulated spectra that have *not been convolved* with a COS-like line-spread function to avoid a potential bias between intrinsic/physical- and spectral properties (e.g. between the gas temperature and the corresponding line width; see Figure A1). Next, we extract subsets from our sample of Ne VIII absorbers chosen in terms of various $N_{\text{Ne VIII}}$, τ_0 , and W_r cuts, and compute for each of these Ne VIII absorbers a characteristic (i.e. Ne VIII optical depth weighted) density n_{H} and a characteristic temperature T , as described in Section 2.1. We finally adjust c_L in our analytic model (equations 7, 9, 10, and 11) to simultaneously reproduce the distribution of each of these subsets on the $n_{\text{H}} - T$ plane.

We find that $\log_{10} c_L = -0.5$ (i.e. $c_L \approx 0.3$) yields very satisfactory results, adopting our fiducial values $[\text{Ne}/\text{H}] = -0.7$ and $f_g = 0.168$, as shown in Figure 2. The panel on the top-right of this figure displays a scatter plot of the Ne VIII absorbers identified in our simulated spectra colour-coded for the various $N_{\text{Ne VIII}}$ cuts indicated in the legend. The solid contours indicate the predicted Ne VIII column density as a function of n_{H} and T as given by our analytic model (equation 7). The bottom-left and bottom-right panels display, respectively, a scatter plot of the Ne VIII absorbers colour coded by different Ne VIII central optical depth (τ_0) and rest-frame equivalent width (W_r) cuts. The contours in the corresponding panel show τ_0 as a function of n_{H} and T as given by equation (10) and W_r as a function of n_{H} and T computed using equation (11). The top-left panel displays the distribution of Ne VIII mass in gas as a function of its density and temperature in our simulation and has already been discussed in Section 2.1. The blue curve indicates the minimum column density $N_{\text{Ne VIII}} = 10^{11} \text{ cm}^{-2}$ allowed in our fitting procedure (see Appendix B) and has been computed using equation (7). Note that virtually all the Ne VIII mass in gas is contained within the region on the $n_{\text{H}} - T$ plane defined by this limit. This is important as a consistency check because it implies that we can detect the bulk of the Ne VIII mass in absorption using our synthetic spectra.

The contours in panels 2 - 4 of Figure 2 agree well with the values of the coloured points in the same panels, indicating that our analytic model reproduces the spectral properties of a statistical significant sample of simulated Ne VIII absorbers as a function of the density and temperature of the absorbing gas. While it is true that our fiducial parameter values ($f_g = 0.168$, $\log_{10} c_L = -0.5$, $[\text{Ne}/\text{H}] = -0.7$) may not apply in general to all absorbers, they should still be representative. First, there is no particular reason why the ratio of baryonic to total mass in such systems should be very different from its universal value. Moreover, the value $\log_{10} c_L = -0.5$ yields sizes for the Ne VIII absorbers (see equation 5) on the order of $10 - 10^2$ kpc, which are consistent with the typical size of Ne VIII absorbers around haloes both in observations (Meiring et al. 2012) and in other simulations (Ford et al. 2012). Values $c_L \ll 1$ are also consistent with observations of C IV absorbers at high redshift (Schaye et al. 2007). And finally, the fiducial value of the neon abundance is broadly consistent with the currently measured abundances of Ne VIII absorbers at low redshift.

In principle, higher values of $[\text{Ne}/\text{H}]$ and lower values of c_L are both allowed by observations. Within the framework of our model, however, these parameters are not completely independent

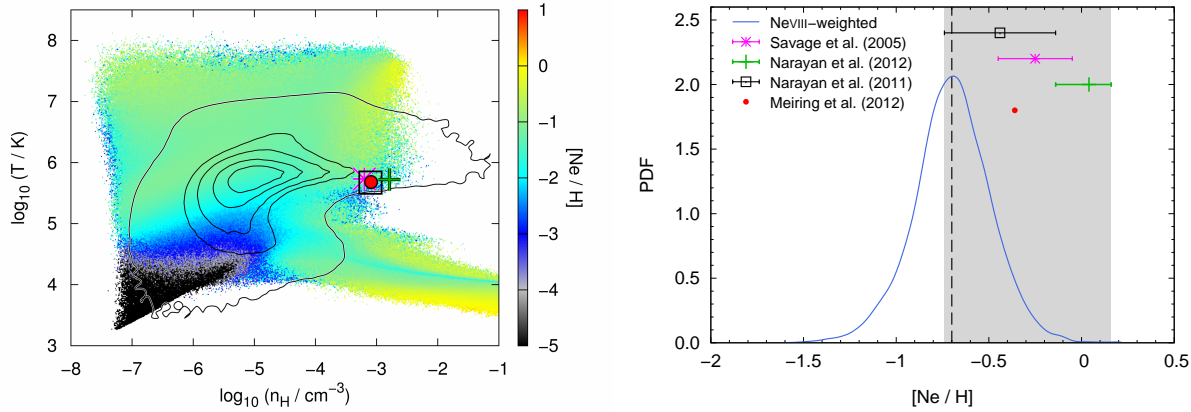


Figure 7. Neon abundance, $[\text{Ne}/\text{H}] \equiv \log_{10}(n_{\text{Ne}}/n_{\text{H}}) - \log_{10}(n_{\text{Ne}}/n_{\text{H}})_{\odot}$, in gas in our simulation at $z = 0.5$. *Left:* Mass-weighted mean of $[\text{Ne}/\text{H}]$ in gas as a function of the gas density and gas temperature. The black contours indicate the distribution of Ne VIII mass in gas, and they correspond to the distribution shown in colour in Figure 8. *Right:* Distribution of $[\text{Ne}/\text{H}]$ values in Ne VIII absorbing gas in our simulation (blue curve). The vertical dashed line indicates the corresponding median value $[\text{Ne}/\text{H}] = -0.7$, which is also the fiducial value adopted in our analytic model. The shaded area indicates the full range of neon abundances measured in Ne VIII absorbers at low redshift (see Table 1). The data points in both panels represent a subset of the observed Ne VIII absorbers listed in Table 1. Note that their measured neon abundances (right panel) are broadly consistent with the mean neon abundance of the gas in our simulation at the corresponding densities and temperatures (left panel). All abundances are given relative to $\log_{10}(n_{\text{Ne}}/n_{\text{H}})_{\odot} = -3.91$.

of each other. For instance, if we demand that our analytic model yields quantitatively the same results in order to remain consistent with our simulation, then a higher neon abundance requires a lower value of c_L for a given n_{H} and T . In other words, our analytic model predicts that at a given Ne VIII column density, high (low) metallicity absorbers are more compact (extended), on average.

Needless to say, it is not the *exact* value of c_L (nor of $[\text{Ne}/\text{H}]$), but its order of magnitude that is important as a parameter that quantifies the degree of metal mixing in gas. The power of our analytic model ultimately lies in providing a connection between the observable parameters ($N_{\text{Ne VIII}}, W_r, N_{\text{H}}$) and the physical parameters ($n_{\text{H}}, T, N_{\text{H}}, [\text{M}/\text{H}], l$) of the absorbing gas, while accounting for the observed inhomogeneous distribution of metals.

3 SPECTRAL SIGNATURES OF Ne VIII ABSORBING GAS

Now that we have found sensible values for the parameters entering our analytic model, we use it, in combination with our simulation, to analyse the connection between the spectral characteristics and the physical state of Ne VIII absorbing gas at $z = 0.5$. The results are shown in Figure 8 and discussed below.

Each of the panels in this figure displays a series of contours that show the behaviour predicted by our analytic model for Ne VIII absorbers as a function of the density and temperature of the Ne VIII absorbing gas. The physical parameter we consider are: the Ne VIII column density (top-left), the Ne VIII rest-frame equivalent width (top-right), the Ne VIII central optical depth (middle-left), the minimum S/N (at 5σ significance) required to detect Ne VIII absorbing gas assuming the line to be fully resolved (middle-right), the total hydrogen column density N_{H} (bottom-left), and the neutral hydrogen column density N_{H_1} (bottom-right) of the Ne VIII bearing gas. The alternative y -axis in the top-right panel indicates the thermal broadening of a Ne VIII absorption line (equation 9). The dashed lines in the middle-right panel indicate the approximate size (in kpc) across the Ne VIII absorber, given by equation (5). The column density, the central optical depth, and the rest-frame equivalent width are computed using equations (7), (10), and (11), respectively, adopting

$\log_{10} c_L = -0.5$ (i.e. $c_L \approx 0.3$) and the fiducial values $[\text{Ne}/\text{H}] = -0.7$ and $f_g = 0.168$. The coloured areas (which are identical in all panels) show the distribution of Ne VIII mass in gas in our simulation at $z = 0.5$ and have already been discussed in Section 2.1. Note that they are identical to the distribution shown in colour in the top-left panel of Figure 2.

We first give a few comments on the qualitative trends seen in each of the panels in Figure 8. Quite apparent is the similarity between the behaviour of the Ne VIII ion fraction ($f_{\text{Ne VIII}}$; Figure 1) and the behaviour of each of the line observables with n_{H} and T , indicating that $f_{\text{Ne VIII}}$ is the dominant factor in setting the absorption signatures of the absorbing gas. Yet, the correspondence is not perfect. In particular, we see that despite the relatively high ion fraction $f_{\text{Ne VIII}} \sim 0.1$ of low-density, photo-ionised gas with $n_{\text{H}} \sim 10^{-6} \text{ cm}^{-3}$ and $T \sim 10^4 \text{ K}$, the corresponding Ne VIII column density is low, $N_{\text{Ne VIII}} \sim 10^{12} \text{ cm}^{-2}$, compared to the Ne VIII column density $N_{\text{Ne VIII}} \sim 10^{14} \text{ cm}^{-2}$ of gas with $n_{\text{H}} \sim 10^{-4} \text{ cm}^{-3}$ and $T > 10^5 \text{ K}$. This can be understood in terms of equation (7), which predicts that, for a fixed $f_{\text{Ne VIII}}$ and a fixed neon abundance, the Ne VIII column density scales as $N_{\text{Ne VIII}} \propto n_{\text{H}} l \propto (n_{\text{H}} T)^{1/2}$. As a result, the Ne VIII column density of photo-ionised gas at $n_{\text{H}} < 10^{-5} \text{ cm}^{-3}$ and $T < 10^5 \text{ K}$ can be orders of magnitude lower than the Ne VIII column density of collisionally ionised gas with $n_{\text{H}} > 10^{-5} \text{ cm}^{-3}$ and $T \approx 5 \times 10^5 \text{ K}$, even though $f_{\text{Ne VIII}} \sim 0.1$ in both gas phases and even if we assume identical metallicities. The equivalent width (W_r ; top-right panel) of the Ne VIII absorbing features produced by these gas phases behaves in a similar way, since for $N_{\text{Ne VIII}} \lesssim 10^{14} \text{ cm}^{-2}$, which is the case of much of the gas in the range of densities and temperatures shown, W_r is directly proportional to $N_{\text{Ne VIII}}$ (see right panel of Figure A1).

The optical depth (middle-left panel) of the gas shows a slightly different behaviour. For instance, the optical depth at the line centre of Ne VIII absorbers produced in photo-ionised and collisionally ionised gas is comparable, $\tau_0 \gtrsim 0.1$, even though the corresponding column densities are an order of magnitude apart. This can be explained as follows: At temperatures $T < 10^5 \text{ K}$ the Ne VIII absorption lines are expected to be narrow ($b_{\text{Ne VIII}} \ll 10 \text{ km s}^{-1}$; see right y -axis in top-right panel) if their width is dominated by thermal broadening.

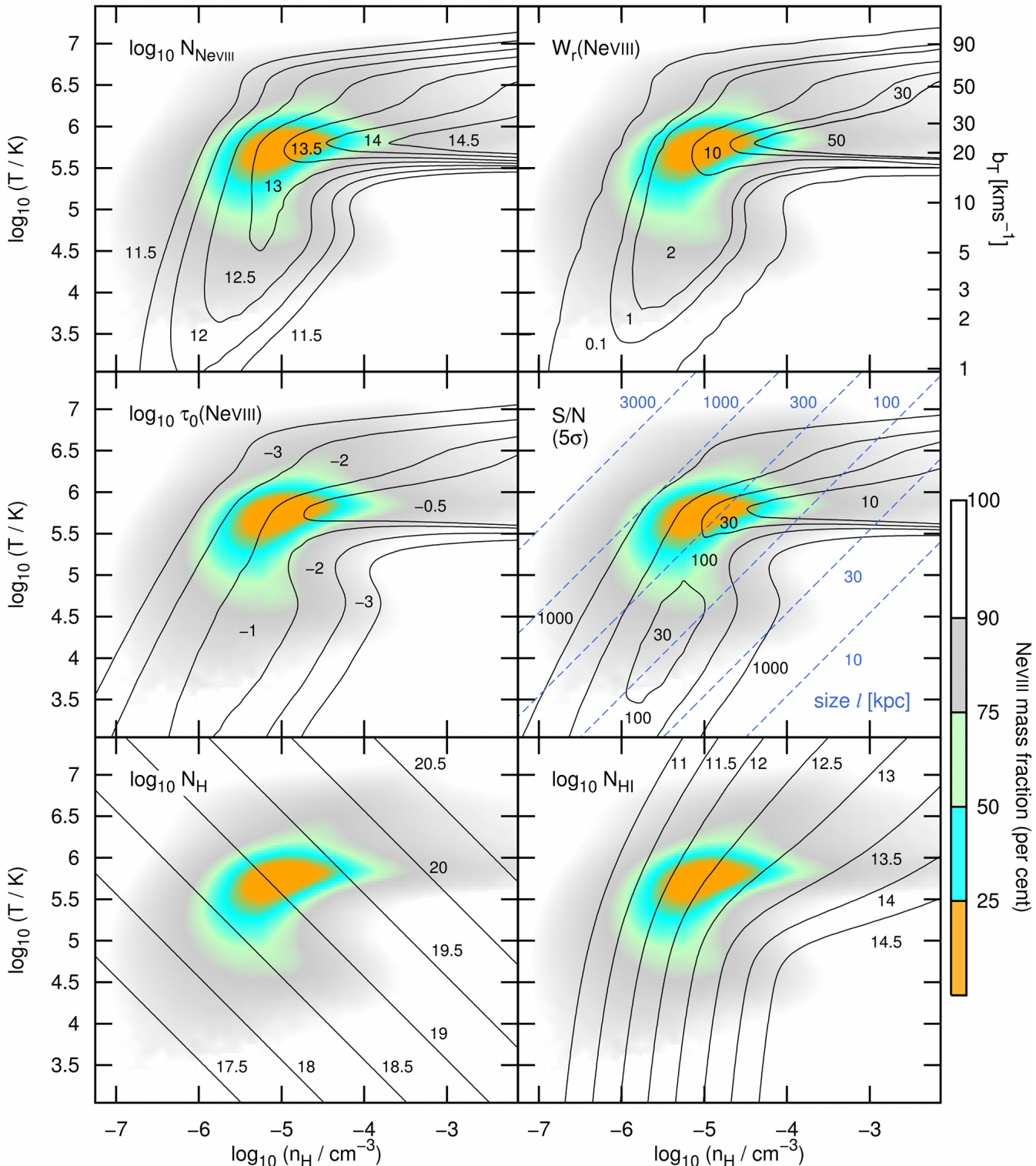


Figure 8. Ne VIII line observables and mass distribution of Ne VIII in gas at $z = 0.5$ as a function of hydrogen particle density (n_H) and temperature (T). The coloured regions show the fraction of Ne VIII mass in the simulation indicated by the colour bar on the bottom-right margin, and they are identical in all panels (and correspond to the coloured regions shown in Figure 2). The contours in each panel show the predictions of our analytic model. *Top-left:* Ne VIII column density ($N_{\text{Ne VIII}}$ in cm^{-2}) as given by equation (7). *Top-right:* Rest-frame equivalent width (in $\text{m}\text{\AA}$) of a Ne VIII absorption line computed using equation (11). The right y -axis in this panel indicates the corresponding thermal broadening (equation 9). *Middle-left:* Ne VIII central optical depth (τ_0) as given by equation (10). *Middle-right:* Minimum S/N required to detect Ne VIII absorbing gas calculated assuming a 5σ significance, assuming the line to be fully resolved. The dashed contours indicate the approximate size (in kpc) across the Ne VIII absorber. *Bottom-left:* Total hydrogen column density (N_H in cm^{-2}) of Ne VIII bearing gas (equation 13). *Bottom-right:* Neutral hydrogen column density (N_{HI} in cm^{-2}) of Ne VIII bearing gas (equation 14). Note that the total H and H I column densities of the gas clouds that harbour the metal patches are a factor c_L^{-1} greater. The contours shown in all panels have been computed assuming a neon abundance $[\text{Ne}/\text{H}] = -0.7$ (relative to $\log_{10}(n_{\text{Ne}}/n_{\text{H}})_\odot = -3.91$), a gas fraction $f_g = 0.168$, and a line of sight metal filling fraction $\log_{10} c_L = -0.5$ (i.e. $c_L \approx 0.3$). Note that the contour values are given on a logarithmic scale in all the panels on the left and in the bottom, and on a linear scale in the others.

Since $\tau_0 \propto (N_{\text{Ne VIII}}/b_{\text{Ne VIII}})$, a decrease in $N_{\text{Ne VIII}}$ is counterbalanced by a decrease in $b_{\text{Ne VIII}}$ such that τ_0 remains approximately constant. Since the minimum S/N value required to detect Ne VIII in gas at a given density and temperature scales as $(\tau_0)^{-1}$ (see equation 12), there is a natural correspondence between low (high) optical depths of the Ne VIII absorbing gas and the high (low) S/N values required to detect such gas, as can be seen by comparing the middle panels with each other.

Finally, the total hydrogen column density N_{H} scales as $(n_{\text{H}}T)^{1/2}$ (see equation 13), which explains the linear (increasing) behaviour of $\log_{10} N_{\text{H}}$ with $\log_{10} n_{\text{H}} (\log_{10} T)$ for a fixed $T (n_{\text{H}})$ as seen in the bottom-left panel. Likewise, the typical linear size across the Ne VIII absorber shown by the blue dashed lines in the middle-right panel obeys $l \propto L_J \propto (T/n_{\text{H}})^{1/2}$, thus linearly increasing (decreasing) with $\log_{10} T (\log_{10} n_{\text{H}})$. The behaviour of N_{H} is dictated by the non-trivial dependence of f_{H1} on n_{H} , and particularly on T (see equation A7 of Schaye 2001, and Figure 7 of Tepper-García et al. 2012).

Further insight into the nature of Ne VIII absorbers at low redshift can be obtained by comparing the distribution of Ne VIII mass in gas in our simulation (coloured regions) with the spectral properties of the gas as a function of its density and temperature predicted by our analytic model (contours) shown in each panel. We see that in our model universe most of the Ne VIII mass is contained in gas with densities $\log_{10}(n_{\text{H}}/\text{cm}^{-3}) \lesssim -4$ (corresponding to overdensities $\Delta \lesssim 150$ at $z = 0.5$) and temperatures $T \lesssim 10^6 \text{ K}$ for which the Ne VIII column densities are expected to be $N_{\text{Ne VIII}} \lesssim 10^{14} \text{ cm}^{-2}$ and the corresponding rest-frame equivalent widths $W_r \lesssim 30 \text{ m}\text{\AA}$. This result is consistent with the distribution of column densities and equivalent widths obtained from our synthetic spectra (Section 2.1.2). The gas containing most of the Ne VIII mass in our simulation thus produces weak to moderate Ne VIII absorption features with optical depths at the centre $\log_{10} \tau_0 < -0.5$; therefore, S/N values of 30 or higher are required to detect these features (at 5σ significance). The line widths implied by the corresponding gas temperatures, if thermal broadening dominates, are $b_{\text{Ne VIII}} < 30 \text{ km s}^{-1}$, with most of the Ne VIII mass in gas producing thermally broadened lines with $10 \text{ km s}^{-1} < b_{\text{Ne VIII}} < 30 \text{ km s}^{-1}$. The gas responsible for the Ne VIII absorption produces H I absorption displaying a wide range of H I column densities: $10^{11} < (N_{\text{H1}}/\text{cm}^{-2}) < 10^{14}$. The average baryon content of this gas in the form of hydrogen corresponds to total column densities $\log_{10}(N_{\text{H}}/\text{cm}^{-2}) < 19.5$.

We find that only a small fraction of the Ne VIII mass in our simulation resides in gas with densities $n_{\text{H}} \gtrsim 10^{-4} \text{ cm}^{-3}$ and temperatures around $T \approx 5 \times 10^5 \text{ K}$, i.e. in gas which produces Ne VIII absorption with column densities $N_{\text{Ne VIII}} \gtrsim 10^{14} \text{ cm}^{-2}$ (and $W_r > 30 \text{ m}\text{\AA}$). These Ne VIII absorbers should be detectable in absorption in spectra with $\text{S/N} \gtrsim 10$ (at 5σ significance), given that their line strength is $\log_{10} \tau_0 \gtrsim -0.5$. The gas temperatures imply line widths $b_{\text{Ne VIII}} \gtrsim 20 \text{ km s}^{-1}$. The average total hydrogen column densities of the gas responsible for this type of Ne VIII absorption can be as high as $N_{\text{H}} \sim 10^{20} \text{ cm}^{-2}$. Due to the high gas temperatures, the hydrogen neutral fraction in this gas is low, and the gas produces H I absorption of ‘BLA’ type: weak, with column densities $10^{13} \lesssim (N_{\text{H1}}/\text{cm}^{-2}) \lesssim 10^{14}$, and broad, with $b_{\text{H1}} \gtrsim 90 \text{ km s}^{-1}$; a high sensitivity is thus required to detect this gas phase using H I absorption. The linear extent of absorbers with densities $n_{\text{H}} \sim 10^{-4} \text{ cm}^{-3}$ and temperatures $T < 10^6 \text{ K}$ is on the order of 10^2 kpc , and it decreases with density. Note, however, that the size, and the H and H I column densities of the gas clouds that *harbour* the metal cloudlets responsible for the Ne VIII absorption are a factor c_L^{-1} higher. It is worth noting that all these properties closely resemble the properties

of the Ne VIII absorbers at low redshift reported in the literature to date. We will discuss this in more detail in the next section.

Our analytic model, in combination with our simulation, therefore predicts that Ne VIII absorbers with $N_{\text{Ne VIII}} \gtrsim 10^{14} \text{ cm}^{-2}$ (and $W_r \gtrsim 30 \text{ m}\text{\AA}$) are not common at low redshift. However, the weakest members in this class of Ne VIII absorbers are just strong enough to allow their detection in absorption spectra with $\text{S/N} \sim 10$. The detection of weaker, but more common Ne VIII absorbers requires a significantly higher sensitivity $\text{S/N} \sim 100$. Our model thus simultaneously provides a natural explanation for the low detection rate of Ne VIII absorbers at low redshift –first noted by Narayanan et al. (2012)–, as well as for the similarity in their strength ($N_{\text{Ne VIII}} \sim 10^{14} \text{ cm}^{-2}$) given that the typical sensitivity of common UV spectra is $\text{S/N} \sim 10$ (see Section 4).

Equally important, the result from our model that absorbers with $N_{\text{Ne VIII}} \gtrsim 10^{14} \text{ cm}^{-2}$ and $W_r > 30 \text{ m}\text{\AA}$ are only produced in gas with temperatures in a very narrow range around $T \approx 5 \times 10^5 \text{ K}$ strongly supports the idea that *this* particular class of Ne VIII absorbers is a sensitive probe of the gas temperature (Savage et al. 2005). In other words, the detection of Ne VIII absorbers with $N_{\text{Ne VIII}} \gtrsim 10^{14} \text{ cm}^{-2}$ is a strong indication of the presence of gas with temperatures $\log_{10}(T/\text{K}) \gtrsim 5.5$, *under ionisation equilibrium conditions*.

Our model further predicts that the gas that produces such strong Ne VIII absorption can have total hydrogen column densities $N_{\text{H}} \gg 10^{19} \text{ cm}^{-2}$. Nevertheless, the overall baryon content of low-redshift Ne VIII absorbers may not be as high as had been expected (e.g. Savage et al. 2005). Indeed, the total baryon content of the gas producing the Ne VIII absorption in our simulation amounts to $\Omega_b(\text{Ne VIII}) = 1.22 \times 10^{-3}$ or roughly 3 per cent of the total baryon budget. The gas producing absorbers with $N_{\text{Ne VIII}} \gtrsim 10^{14} \text{ cm}^{-2}$ contain less than 0.5 per cent of the total baryons. Note, however, that our estimate represents a strict lower limit, since we ignore absorbers with $N_{\text{Ne VIII}} \lesssim 10^{12} \text{ cm}^{-2}$ which contain roughly 20 per cent of the Ne VIII mass in our simulation (see Section 2.1.2), although according to our model predictions their average total hydrogen column densities, and in consequence their baryon content, is expected to be relatively low, $N_{\text{H}} < 10^{18} \text{ cm}^{-2}$. Note also that the *total* baryon density *traced* by the Ne VIII absorbers is a factor c_L^{-1} higher, or approximately 10 per cent of the total baryon budget in our simulation if $c_L \approx 0.3$. Our result is of the same order as the corresponding value $\Omega_b(\text{Ne VIII}) = 2.63 \times 10^{-3}$ (or 6 per cent of the total baryons in the Universe if $\Omega_b = 0.0418$) estimated by Narayanan et al. (2009), based on a single detection, and the value $\Omega_b(\text{Ne VIII}) = 2.00 \times 10^{-3}$ (roughly 4 per cent of the baryon density if $\Omega_b = 0.0418$) obtained by Meiring et al. (2012) based on three detections.

On the other hand, if $c_L < 0.3$, then the baryon content traced by Ne VIII in our simulation could be significantly higher. For instance, if $c_L \sim 0.1$ as is suggested by observations in combination with our analytic model (see Section 4), then the fraction of the total baryon contained in the (warm-hot) gas harbouring the Ne VIII would be boosted to roughly 30 per cent, which is comparable to the fraction of baryons in gas traced by BLAs in our simulation (25 per cent; Tepper-García et al. 2012). In this case, however, it is unclear what the overlap between BLAs and Ne VIII is in terms of the baryons traced by these ions, and in consequence the true baryon content of warm-hot diffuse gas at low redshift remains uncertain.

Table 1. Summary of Ne VIII detections at $z < 1$. See text for details on the notes. List of references: (1) Savage et al. (2005); (2) Narayanan et al. (2009); (3) Narayanan et al. (2011); (4) Narayanan et al. (2012); (5) Meiring et al. (2012); (6) Savage et al. (2011); (7) Tripp et al. (2011).

QSO	z_{abs}	$\log_{10}(N_{\text{Ne VIII}})^a$ [cm $^{-2}$]	$b_{\text{Ne VIII}}^a$ [km s $^{-1}$]	$W_r(\text{Ne VIII})^c$ [mÅ]	$\log_{10} n_{\text{H}}^f$ [cm $^{-3}$]	$\log_{10}(T)$ [K]	[Ne/H] g	$\log_{10}(N_{\text{H}})$ [cm $^{-2}$]	$\log_{10}(N_{\text{H1}})$ [cm $^{-2}$]	Size [kpc]	Ref.
HE 0226-4110	0.207	13.89 ± 0.11	22.6 ± 15.0	36 ± 10	-3.20	5.68	-0.25	20.06	13.87	60	(1,6)
3C 263	0.326	14.06 ± 0.08	52.4 ± 8.8	57 ± 10	-2.79	5.72	0.04	19.48	13.09	6	(2,4)
PKS 0405-123	0.495	13.96 ± 0.06^b	—	45 ± 6^b	-3.10 ^d	5.67 ^d	-0.44	19.70 ^d	13.50	20 ^e	(3)
PG 1148+549	0.684	13.95 ± 0.04	32.0 ± 5.0	43 ± 4	-3.09	5.68	-0.36	19.80	13.65	10	(5)
PG 1148+549	0.705	13.86 ± 0.05	27.8 ± 3.5	35 ± 4	-2.34	5.69	0.14	19.15	12.90	1	(5)
PG 1148+549	0.725	13.81 ± 0.07	41.4 ± 7.5	33 ± 5	-3.96	5.72	0.14	18.83	13.08	20	(5)
PG 1206+459	0.927	13.71 ± 0.29	—	—	—	5.56	—	19.80	—	—	(7)
PG 1206+459	0.927	14.04 ± 0.08	—	—	—	5.60	—	20.30	—	—	(7)
PG 1206+459	0.927	14.53 ± 0.04^h	—	—	—	5.65	—	20.50	—	—	(7)

^a Measured using Gaussian profile fitting, unless stated otherwise.

^b Measured using the apparent optical depth method (AOD; Savage & Sembach 1991).

^c Computed here using the measured column density and Doppler parameter assuming a Voigt-profile, unless stated otherwise.

^d Estimated assuming photo- and collisional ionisation equilibrium.

^e Inferred from the total hydrogen column density N_{H} and n_{H} using $l = N_{\text{H}}/n_{\text{H}}$.

^f Estimated here from the inferred size l of the photo-ionised phase and N_{H} using $n_{\text{H}} = N_{\text{H}}/l$.

^g Relative to $\log_{10}(n_{\text{Ne}}/n_{\text{H}})_{\odot} = -3.91$.

^h Total column density of a two-component feature.

4 COMPARISON WITH OBSERVATIONS

Given the relevance of the results presented in the previous section, it is important to test the predictions from our analytic model using the measured (and inferred) properties of Ne VIII absorbers observed at low redshift. In Table 1 we present all the Ne VIII detections available in the literature to date, listing only those physical parameters that are relevant for our study (if available). Unless stated otherwise, all the values listed in Table 1 are taken from the corresponding reference given in the last column.

In some cases (e.g. Savage et al. 2005; Meiring et al. 2012), the gas temperature of the collisionally ionised gas phase responsible for the Ne VIII and O VI absorption has been obtained by scaling N_{H} in order for the model to reproduce the measured Ne VIII and O VI column densities, assuming CIE and some value for the metallicity (usually the same value of the metallicity inferred for the photo-ionised gas phase). In these cases, N_{H1} has been calculated from the inferred temperature which sets the H I ionisation fraction f_{H1} (assuming CIE) and the inferred N_{H} using $N_{\text{H1}} = f_{\text{H1}} N_{\text{H}}$.

In others cases (e.g. Narayanan et al. 2012), the gas temperature of the observed Ne VIII absorbing gas has been inferred from the ratio of the observed Ne VIII to O VI column densities ($N_{\text{Ne VIII}}/N_{\text{O VI}}$) assuming CIE and fixed (e.g. solar) abundances. The inferred temperature (together with the assumption of CIE) has then been used to convert the measured neutral hydrogen column density (N_{H1}) into a total hydrogen column density (N_{H}). In these cases, the H I column density of the gas phase responsible for the Ne VIII and O VI absorption has been either directly measured in the spectrum (e.g. Savage et al. 2011) or estimated by overlaying onto the H I absorption feature detected in the observed spectrum an additional H I component whose width is set by the inferred gas temperature and whose H I column density is the largest possible such that the overall fit is still consistent with the data (e.g. Narayanan et al. 2011, 2012).

With one notable exception, there are no estimates (apart from upper or lower limits) of the density of the Ne VIII absorbers available in the literature. The only estimate is given by Naray-

anan et al. (2011) for a Ne VIII absorber at $z \approx 0.5$. They obtain $\log_{10}(n_{\text{H}}/\text{cm}^{-3}) = -3.10$ using a model that combines the effects of photo- and collisional ionisation (as opposed to assuming CIE only) to compute the ionisation balance of the absorbing gas, which is the same approach we use here (see Appendix A for more details on the analysis of this absorbing system). We therefore consider their measurements to be the most suitable for comparison with the results from our analytic model. As for the other observed Ne VIII absorbers, and with no other choice at hand, we compute the gas density from the inferred size (l) and the total hydrogen density (N_{H}) using the simple relation $n_{\text{H}} = N_{\text{H}}/l$, whenever possible. Note that l refers to the linear extension of the photo-ionised component inferred by assuming photo-ionisation equilibrium (PIE) while N_{H} refers to the total hydrogen column density of the associated collisionally ionised gas phase.

Finally, in order to be self-consistent, we compute the rest-frame equivalent width (rather than using its measured value) with the help of equations (1) and (11) using the values for the Ne VIII column density ($N_{\text{Ne VIII}}$) and the Doppler parameter ($b_{\text{Ne VIII}}$) obtained by each group from line-profile fitting.

Figure 9 shows the comparison of the physical parameters predicted by our analytic model to the corresponding measured and inferred parameters of the Ne VIII absorbers listed in Table 1. Note that we use only the subset of the observations for which we have an estimate of the gas density (n_{H}). The panels in this figure display a series of contours which show, from the top-left and moving clockwise, the Ne VIII column density ($N_{\text{Ne VIII}}$), the rest-frame Ne VIII equivalent width (W_r), the total hydrogen column density (N_{H} ; black lines) and the neutral hydrogen column density (N_{H1} ; blue curves) of the Ne VIII absorbing gas, and the minimum required sensitivity (in terms of S/N) to detect gas using Ne VIII absorption as a function of the gas density and temperature, assuming the line to be fully resolved. The top-right panel shows additionally the approximate size (in kpc) across the Ne VIII absorber (blue dashed lines). Note that the contours are identical to the corresponding contours shown in Figure 8. The data points represent the observed Ne VIII absorbers.

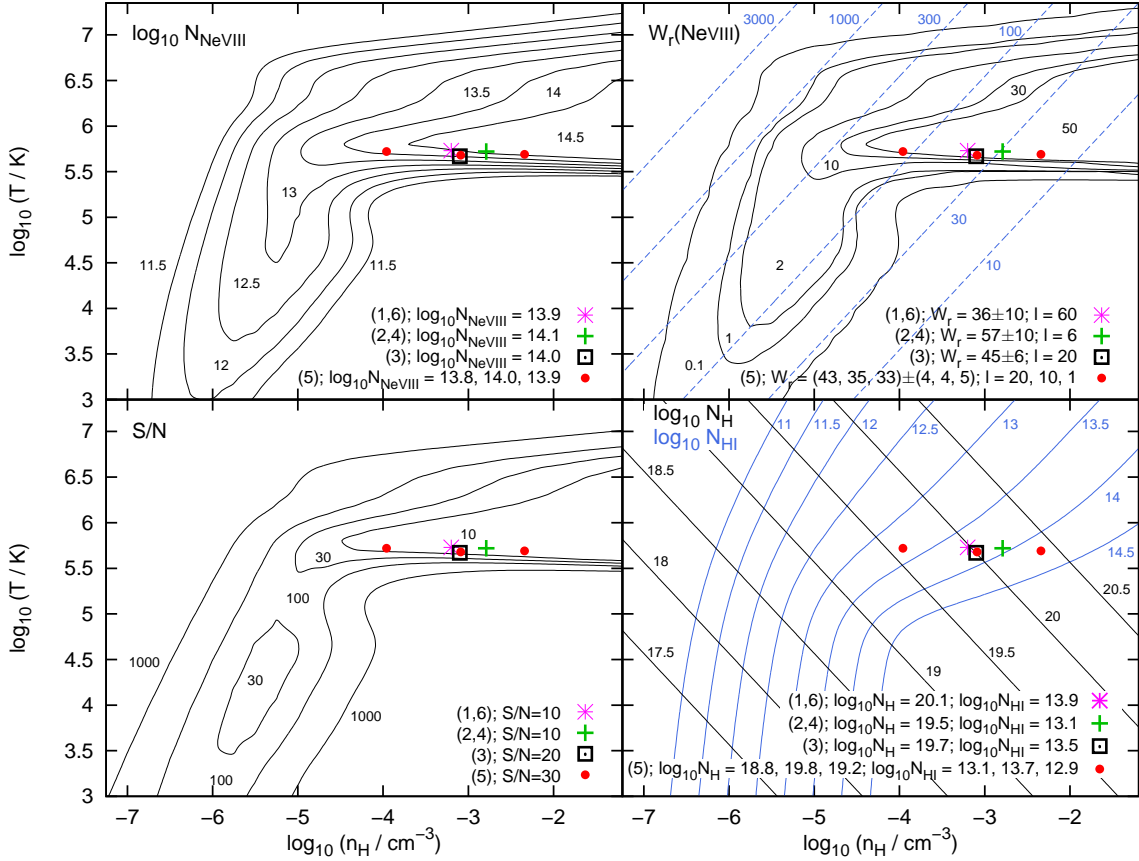


Figure 9. Comparison of the spectral and physical properties predicted by our analytic model to the corresponding measured and inferred properties of a sample of observed Ne VIII absorbers at low redshift as reported in the literature: Ne VIII column density ($N_{\text{Ne VIII}}$; top-left), Ne VIII rest-frame equivalent width (W_r ; top-right; black contours) and linear size in kpc (l ; top-right; blue dashed lines), total hydrogen column density (N_{H} ; bottom-right; black lines) and neutral hydrogen column density (N_{H1} ; bottom-right; blue curves). The contours in the bottom-left panel show the minimum sensitivity in terms of S/N required to detect gas at a given density and temperature using resolved Ne VIII absorption at 5σ significance. The values for each quantity measured (or inferred) from observations are indicated in the legend along with their corresponding reference. A complete list of the quantities measured and inferred from observations is given in Table 1. The S/N values quoted in the bottom-left panel correspond to the average S/N of the data in the spectral range of interest. Note that the contours in each panel are identical to the corresponding contours shown in Figure 8. List of references: (1) Savage et al. (2005); (2) Narayanan et al. (2009); (3) Narayanan et al. (2011); (4) Narayanan et al. (2012); (5) Meiring et al. (2012); (6) Savage et al. (2011).

In each panel, the measured (or inferred) value of a given physical parameter (e.g. $N_{\text{Ne VIII}}$) is indicated in the legend, along with the reference it has been taken from (see the figure caption and Table 1).

We find broad agreement between the results inferred from observations and the predictions from our analytic model. The panels in the top row, for instance, demonstrate that the measured Ne VIII column densities, as well as the measured rest-frame Ne VIII equivalent widths, of the observed Ne VIII absorbers with a given inferred density and inferred temperature fall within the range of Ne VIII column densities and equivalent widths predicted by our model for gas in the corresponding density and temperature range. It is remarkable that all the observed Ne VIII absorbers have very similar strengths, $N_{\text{Ne VIII}} \sim 10^{14} \text{ cm}^{-2}$, within the given uncertainties, and that they have all been detected in spectra with (average) $\text{S/N} \sim 10$,

which is perfectly consistent with the result from our model (compare top-left and bottom-left panels). The bottom-right panel shows that both the ranges of H and H1 column densities of the gas responsible for the Ne VIII absorption obtained from observations are well predicted by our analytic model. Also, the typical linear extension of the absorbers resulting from our model is broadly consistent with the sizes inferred from observations (see top-right panel). The worst agreement between our model predictions and the corresponding results obtained from observations, in particular for l , is shown by the Ne VIII absorbers at $z = 0.705$ and $z = 0.725$ reported by Meiring et al. (2012, left and right red dots). Some of the discrepancy may come from the fact that our model curves are computed assuming $[\text{Ne}/\text{H}] = -0.7$, whereas these two observed Ne VIII absorbers have higher (super-solar) abundances $[\text{Ne}/\text{H}] = 0.14$ (relative to $\log_{10} (n_{\text{Ne}}/n_{\text{H}})_{\odot} = -3.91$). In contrast, all the measured properties

of the $z = 0.495$ Ne VIII absorber detected by Narayanan et al. (2011, black square) are almost perfectly reproduced by our analytic model, although the neon abundance in this absorbers is also inferred to be higher, $[\text{Ne}/\text{H}] = -0.44$, than our adopted value, $[\text{Ne}/\text{H}] = -0.7$.

The fact that the average neon abundance of the observed Ne VIII absorbers ($[\text{Ne}/\text{H}] \approx -0.2$; see Figure 7) is higher by 0.5 dex than the fiducial value of our analytic model has an interesting implication. As discussed in Section 2.2.1, consistency between our analytic model and our simulation demands that c_L decreases (increases) if $[\text{Ne}/\text{H}]$ increases (decreases). More precisely, increasing the value of $[\text{Ne}/\text{H}]$ by 0.5 dex higher would require us to decrease $\log_{10} c_L$ by the same amount. Therefore, adopting $[\text{Ne}/\text{H}] = -0.2$ would require $\log_{10} c_L = -1$. In other words, the typical neon abundance observed in low redshift Ne VIII absorbers, in combination with our analytic model, favours values $c_L \sim 10^{-1}$, thus supporting the idea that metals are in-homogeneously distributed at low redshift. Such a change in the values of $[\text{Ne}/\text{H}]$ and c_L would leave the predicted values for $N_{\text{Ne VIII}}$ and W_r (top-row panels of Figure 9) unaltered, but it would reduce the predicted sizes l , and the gas column densities N_{H} and N_{H_1} by a factor $10^{0.5} \approx 3$, all of which would still be consistent with the results inferred from observations. Note that, in particular, the predicted sizes of absorbers with $N_{\text{Ne VIII}} \sim 10^{14} \text{ cm}^{-2}$ would be on the order of 10 kpc.

It is noteworthy that the inferred gas temperature of all observed Ne VIII absorbers is very similar and close to the temperature $T \approx 5 \times 10^5 \text{ K}$ at which the Ne VIII fraction peaks in CIE. In contrast, their densities span almost two orders of magnitude. However, if we ignore the metal-rich Ne VIII absorbers detected by Meiring et al. (2012), then all Ne VIII absorbers observed at low redshift appear to be produced under rather uniform physical conditions, that is in gas with $n_{\text{H}} \sim 10^{-3} \text{ cm}^{-3}$ and $T \approx 5 \times 10^5 \text{ K}$, and total hydrogen column densities $N_{\text{H}} \sim 10^{20} \text{ cm}^{-2}$. The relatively high densities of the observed Ne VIII absorbers, which correspond to overdensities of $\Delta \approx 1.5 \times 10^3$ at $z = 0.5$, indicate that they likely originate in the immediate vicinity of galaxies.

It is important to stress that we do not expect a perfect agreement between our analytic model and the observations for several reasons. First, an accurate comparison of the predicted and measured column densities and equivalent widths is difficult, given that our model assumes the lines to be fully resolved while the intrinsic velocity structure of the observed lines may be blurred by the limited resolution and sensitivity (S/N) of the data, as demonstrated for instance in Figure 4. Second, the physical parameters of the Ne VIII absorbers obtained from observations are based on models that assume collisional ionisation equilibrium (but see Narayanan et al. 2011), while we take both the effect both of photo- and collisional ionisation into account to compute the ionisation balance of the absorbing gas (although we also assume ionisation equilibrium). Furthermore, the gas densities (n_{H}) of the observed Ne VIII absorbers, which we have computed from the inferred total hydrogen column densities (N_{H}) and the size (l) of the photo-ionised gas phase, are uncertain due to the uncertainties in both N_{H} and l . Also, the sizes predicted by our model correspond to those of the metal clouddlets, and these may be smaller than those of the gas clouds in which the metal clouddlets are embedded if the metals are poorly mixed on small scales, as we have assumed here. Finally, our analytic model assumes local hydrostatic equilibrium (Schaye 2001) which may hold only approximately and not necessarily for all absorbers.

In spite of these uncertainties, we find that our analytic model broadly reproduces the properties of observed Ne VIII absorbers at low redshift, although the number of current detections is still small. Thus, more data is required before we can test the predictions of

our model in a more robust way. Such data should soon become available from the analysis of a large sample of high-quality spectra obtained with COS.

The results presented above lead us to conclude that the Ne VIII detections reported to date in the literature likely correspond to collisionally ionised, baryon-rich (in terms of N_{H} with $N_{\text{H}} \sim 10^{20} \text{ cm}^{-2}$), compact (~ 10 kpc) metal absorbers produced in gas with temperatures well above 10^5 K and with densities $n_{\text{H}} \gg 10^{-5} \text{ cm}^{-3}$. These strong Ne VIII absorbers with $N_{\text{Ne VIII}} \sim 10^{14} \text{ cm}^{-2}$ most probably originate close to galaxies, and they make up only a small fraction of the general Ne VIII absorber population at low redshift. The latter consists mainly of weaker Ne VIII absorbers with $N_{\text{Ne VIII}} < 10^{14} \text{ cm}^{-2}$, which are produced in more diffuse gas with hydrogen column densities $N_{\text{H}} \lesssim 10^{19} \text{ cm}^{-2}$, and whose detection requires a sensitivity in terms of S/N on the order of 100.

5 SUMMARY AND CONCLUSIONS

In recent years a substantial fraction of the ultra-violet (UV) spectroscopy of quasars (QSO) has been dedicated to tracking down a peculiar gas phase characterised by its low densities ($n_{\text{H}} \sim 10^{-6} - 10^{-5} \text{ cm}^{-3}$) and relatively high temperatures ($T > 10^5 \text{ K}$) which is expected to harbour a substantial fraction of the baryons in the Universe at low redshift. Next to other ions such as five-times ionised oxygen (O VI) and broad H I Ly α absorbers (BLAs), seven-times ionised neon (Ne VIII) has been considered to be a potential tracer of this gas phase, especially because of the temperature ($T \approx 5 \times 10^5 \text{ K}$) at which the Ne VIII ionisation fraction is highest in collisional ionisation equilibrium. But despite the relatively high abundance of neon in the Universe, there have so far only been a small number of Ne VIII detections at low redshift, and consequently the physical conditions and the fraction of the baryons traced by the gas phase producing the observed Ne VIII absorption are still uncertain.

In this paper we have investigated the physical state of the Ne VIII absorbing gas at low redshift following two independent but complementary approaches. First, we have used a large cosmological simulation of structure formation which includes many of the physical processes relevant to the production and distribution of metals in the Universe. Second, we have developed an analytic model to predict the signatures of Ne VIII absorbing gas as a function of the gas density, temperature, and the abundance of metals in the gas. The assumptions underlying our model are that the metals are in-homogeneously distributed within the gaseous structures responsible for the absorption, that these structures are self-gravitating with sizes of the order of the local Jeans length, that the gas is only exposed to the UV/X-ray background, and that it is in ionisation equilibrium. The last two assumptions were also used in the simulation. We have shown that the simulation and the analytic model are consistent with each other, and that the predictions from our analytic model are broadly consistent with the results from observations, provided that the parameter quantifying the degree of metal mixing along the sightline across the structure, $c_L \sim 10^{-1}$. The parameter c_L corresponds to the fraction of the length of the gas cloud along the line of sight that intersects clouddlets enriched with neon, where the enriched clouddlets have a similar density and temperature as the surrounding gas.

The most important results we obtain from the combination of our simulation and our analytic model regarding the physical state of the Ne VIII absorbing gas at redshift $z = 0.5$ are the following:

(i) High Ne VIII ion fractions $f_{\text{Ne VIII}} \sim 0.1$ can occur both in photo-ionised and collisionally ionised gas, but most of the Ne VIII in our simulation is produced by collisional ionisation in gas with densities $n_{\text{H}} \sim 10^{-5} \text{ cm}^{-3}$ and $T \approx 5 \times 10^5 \text{ K}$ (Section 2.1).

(ii) Ne VIII absorption with Ne VIII column densities $N_{\text{Ne VIII}} \gtrsim 10^{14} \text{ cm}^{-2}$ (or $W_r > 30 \text{ mÅ}$) is only produced in collisionally ionised gas with temperatures around $T = 5 \times 10^5 \text{ K}$ and $n_{\text{H}} \gtrsim 10^{-4} \text{ cm}^{-3}$, total hydrogen column densities $N_{\text{H}} \sim 10^{20} \text{ cm}^{-2}$, and neutral hydrogen column densities $N_{\text{H}_1} \sim 10^{13} - 10^{14} \text{ cm}^{-2}$. The detection of such absorbers is therefore a strong indication of the presence of gas with $T > 10^5 \text{ K}$, provided the gas is in ionisation equilibrium (Section 3).

(iii) At $z = 0.5$ the number of strong Ne VIII ($W_r > 30 \text{ mÅ}$ which corresponds to $N_{\text{Ne VIII}} \gtrsim 10^{14} \text{ cm}^{-2}$) absorbers per unit redshift is predicted to be $dN/dz \sim 10^{-1}$, which is low compared to the total number density of Ne VIII absorbers in our simulation, $dN/dz(W_r > 0.3 \text{ mÅ}) \approx 41$. The more general population of Ne VIII absorbers at low redshift consists of weaker absorbers with $N_{\text{Ne VIII}} \ll 10^{14} \text{ cm}^{-2}$ whose detection requires $\text{S/N} \gtrsim 100$ (Sections 2.1.2, 3).

(iv) At a given Ne VIII column density, the linear extent of the absorbers scales inversely proportional to the metal abundance. Metal-rich ($[\text{Ne}/\text{H}] \approx 0$), strong ($N_{\text{Ne VIII}} \gtrsim 10^{14} \text{ cm}^{-2}$) absorbers have typical sizes $\sim 10 \text{ kpc}$ (Sections 2.1.1, 2.2.1, 4). The gas clouds harbouring these Ne VIII cloudlets are, however, a factor c_L^{-1} larger.

(v) The gas producing the Ne VIII absorption in our simulations contains roughly 3 per cent of the total amount of baryons; absorbers with $N_{\text{Ne VIII}} \gtrsim 10^{14} \text{ cm}^{-2}$ contain less than 0.5 per cent of the total baryons in our simulation. The baryon content of the gas harbouring the Ne VIII absorbers (and which has a similar density and temperature as the Ne VIII cloudlets) is in each case a factor c_L^{-1} higher (Section 3).

(vi) The neon abundances of the Ne VIII absorbing gas in our simulation are distributed in the range $-1.5 \lesssim [\text{Ne}/\text{H}] \lesssim 0$, with median $[\text{Ne}/\text{H}] = -0.7$ (Section 2.2.1).

(vii) The distribution of Ne VIII column densities obtained from synthetic spectra at $z = 0.5$ is well described by a single power law with index $\beta = 2.9 \pm 0.1$, in the range $\log_{10}(N_{\text{Ne VIII}}/\text{cm}^{-2}) \in [12.5, 14.5]$ (Section 2.1.2).

(viii) The small number of Ne VIII absorbers observed at low redshift to date appear to be part of a particular class of scarce, strong ($N_{\text{Ne VIII}} \sim 10^{14} \text{ cm}^{-2}$), baryon-rich ($N_{\text{H}} \sim 10^{20} \text{ cm}^{-2}$), compact ($\sim 10 \text{ kpc}$) metal absorbers produced in gas with densities $n_{\text{H}} \sim 10^{-3} \text{ cm}^{-3}$ and temperatures $T \approx 5 \times 10^5 \text{ K}$. The relatively high densities of these Ne VIII absorbers indicate that they likely originate in the immediate vicinity of galaxies (Section 4).

We conclude that strong Ne VIII absorbers are robust probes of shock-heated diffuse gas. Spectra with signal-to-noise ratio $\sim 10^2$ would allow the detection of the weaker systems that trace a substantial fraction of the baryons at low redshift.

ACKNOWLEDGMENTS

We are grateful to all members of the OWLS team. We acknowledge in particular the contributions of Craig M. Booth and Tom Theuns to SPECWIZARD and the help the former provided in the use of the simulations. The simulations presented here were run on Stella, the LOFAR Blue Gene/L system in Groningen and on the Cosmology Machine at the Institute for Computational Cosmology in Durham as part of the Virgo Consortium research programme. This work was sponsored by the National Computing Facilities Foundation (NCF) for the use of supercomputer facilities, with financial support from the Netherlands Organisation for Scientific Research

(NWO), an NWO VIDI grant, the Marie Curie Initial Training Network CosmoComp (PITN-GA-2009-238356), the *Deutsche Forschungsgemeinschaft* (DFG) through Grant DFG-GZ: Ri 1124/5-1, and the European Research Council under the European Unions Seventh Framework Programme (FP7/2007-2013) / ERC Grant agreement 278594-GasAroundGalaxies.

References

Altay G., Theuns T., Schaye J., Crighton N. H. M., Dalla Vecchia C., 2011, ApJ, 737, L37+

Anders E., Grevesse N., 1989, Geochim. Cosmochim. Acta, 53, 197

Bertone S., Schaye J., Dolag K., 2008, Space Science Reviews, 134, 295

Booth C. M., Schaye J., 2009, MNRAS, 398, 53

Booth C. M., Schaye J., 2011, MNRAS, 413, 1158

Cen R., 2012, ApJ, 753, 17

Cen R., Ostriker J. P., 1999, ApJ, 514, 1

Dalla Vecchia C., Schaye J., 2008, MNRAS, 387, 1431

Danforth C. W., Shull J. M., 2008, ApJ, 679, 194

Danforth C. W., Shull J. M., Rosenberg J. L., Stocke J. T., 2006, ApJ, 640, 716

Danforth C. W., Stocke J. T., Shull J. M., 2010, ApJ, 710, 613

Davé R., Cen R., Ostriker J. P., Bryan G. L., Hernquist L., Katz N., Weinberg D. H., Norman M. L., O’Shea B., 2001, ApJ, 552, 473

Davé R., Hernquist L., Weinberg D. H., Katz N., 1997, ApJ, 477, 21

Ferland G. J., Korista K. T., Verner D. A., Ferguson J. W., Kingdon J. B., Verner E. M., 1998, PASP, 110, 761

Ford A. B., Oppenheimer B. D., Davé R., Katz N., Kollmeier J. A., Weinberg D. H., 2012, ArXiv e-prints

Fukugita M., 2004, in Ryder S., Pisano D., Walker M., Freeman K., eds, Dark Matter in Galaxies Vol. 220 of IAU Symposium, Cosmic Matter Distribution: Cosmic Baryon Budget Revisited. pp 227–+

Green J. C., Froning C. S., Osterman S., Ebbets D., Heap S. H., Leitherer C., Linsky J. L., Savage B. D. e. a., 2012, ApJ, 744, 60

Green J. C., Morse J. A., 1998, Space Telesc. Sci. Inst., Newslett., Vol. 15, No. 1, p. 6 - 7, 21, 15, 6

Haardt F., Madau P., 2001, in D. M. Neumann & J. T. V. Tran ed., Clusters of Galaxies and the High Redshift Universe Observed in X-rays Modelling the UV/X-ray cosmic background with CUBA. CEA, Saclay, p. p. 64

Jarosik N., Bennett C. L., Dunkley J., Gold B., Greason M. R., Halpern M., Hill R. S., Hinshaw e. a., 2011, ApJS, 192, 14

Kramida A. E., Buchet-Poulizac M.-C., 2006, The European Physical Journal D - Atomic, Molecular, Optical and Plasma Physics, 38, 265

Lehner N., Savage B. D., Richter P., Sembach K. R., Tripp T. M., Wakker B. P., 2007, ApJ, 658, 680

Levenberg K., 1944, Q. Appl. Math., 2, 164

Marquardt D., 1963, J. Soc. Ind. Appl. Math., 11, 431

McCarthy I. G., Schaye J., Ponman T. J., Bower R. G., Booth C. M., Dalla Vecchia C., Crain R. A., Springel V., Theuns T., Wiersma R. P. C., 2010, MNRAS, 406, 822

Meiring J. D., Tripp T. M., Werk J. K., Howk C., Jenkins E. B., Prochaska J. X., Lehner N., Sembach K. R., 2012, ArXiv e-prints

Mohr P. J., Taylor B. N., Newell D. B., 2012, Rev. Mod. Phys., 84, 1527

Muzahid S., Srianand R., Savage B. D., Narayanan A., Mohan V., Dewangan G. C., 2012, MNRAS, 424, L59

Narayanan A., Savage B. D., Wakker B. P., 2012, ApJ, 752, 65

Narayanan A., Savage B. D., Wakker B. P., Danforth C. W., Yao Y., Keeney B. A., Shull J. M., Sembach K. R., Froning C. S., Green J. C., 2011, ApJ, 730, 15

Narayanan A., Wakker B. P., Savage B. D., 2009, ApJ, 703, 74

Oppenheimer B. D., Davé R., 2009, MNRAS, 395, 1875

Oppenheimer B. D., Davé R., Katz N., Kollmeier J. A., Weinberg D. H., 2012, MNRAS, 420, 829

Oppenheimer B. D., Schaye J., 2013a, ArXiv e-prints

Oppenheimer B. D., Schaye J., 2013b, ArXiv e-prints

Persic M., Salucci P., 1992, MNRAS, 258, 14P

Press W. H., Teukolsky S. A., Vetterling W. T., Flannery B. P., 1992, Numerical Recipes in Fortran 77, second edn. Cambridge University Press

Prochaska J. X., Weiner B., Chen H.-W., Mulchaey J., Cooksey K., 2011, ApJ, 740, 91

Rahmati A., Pawlik A. P., Raičević M., Schaye J., 2012, ArXiv e-prints

Rauch M., Haehnelt M. G., Steinmetz M., 1997, ApJ, 481, 601

Richter P., Savage B. D., Sembach K. R., Tripp T. M., 2006, A&A, 445, 827

Richter P., Savage B. D., Tripp T. M., Sembach K. R., 2004, ApJS, 153, 165

Savage B. D., Lehner N., Narayanan A., 2011, ApJ, 743, 180

Savage B. D., Lehner N., Wakker B. P., Sembach K. R., Tripp T. M., 2005, The Astrophysical Journal, 626, 776

Savage B. D., Sembach K. R., 1991, ApJ, 379, 245

Schaye J., 2001, ApJ, 559, 507

Schaye J., Aguirre A., Kim T., Theuns T., Rauch M., Sargent W. L. W., 2003, ApJ, 596, 768

Schaye J., Carswell R. F., Kim T., 2007, MNRAS, 379, 1169

Schaye J., Dalla Vecchia C., 2008, MNRAS, 383, 1210

Schaye J., Dalla Vecchia C., Booth C. M., Wiersma R. P. C., Theuns T., Haas M. R., Bertone S., Duffy A. R., McCarthy I. G., van de Voort F., 2010, MNRAS, 402, 1536

Schaye J., Theuns T., Leonard A., Efstathiou G., 1999, MNRAS, 310, 57

Sembach K. R., Tripp T. M., Savage B. D., Richter P., 2004, ApJS, 155, 351

Shull J. M., Smith B. D., Danforth C. W., 2011, ArXiv e-prints

Smith B. D., Hallman E. J., Shull J. M., O'Shea B. W., 2011, ApJ, 731, 6

Spergel D. N., Bean R., Doré O., Nolta M. R., Bennett C. L., Dunkley J., Hinshaw G., Jarosik N. e. a., 2007, ApJS, 170, 377

Springel V., 2005, MNRAS, 364, 1105

Springel V., White S. D. M., Jenkins A., Frenk C. S., Yoshida N., Gao L., Navarro J., Thacker R., Croton D., Helly J., Peacock J. A., Cole S., Thomas P., Couchman H., Evrard A., Colberg J., Pearce F., 2005, Nature, 435, 629

Sutherland R. S., Dopita M. A., 1993, ApJS, 88, 253

Tepper-García T., Richter P., Schaye J., Booth C. M., Dalla Vecchia C., Theuns T., 2012, MNRAS, 425, 1640

Tepper-García T., Richter P., Schaye J., Booth C. M., Dalla Vecchia C., Theuns T., Wiersma R. P. C., 2011, MNRAS, 413, 190

Thom C., Chen H.-W., 2008a, ApJS, 179, 37

Thom C., Chen H.-W., 2008b, ApJ, 683, 22

Tilton E. M., Danforth C. W., Shull J. M., Ross T. L., 2012, ArXiv e-prints

Tripp T. M., Meiring J. D., Prochaska J. X., Willmer C. N. A., Howk J. C., Werk J. K., Jenkins E. B., Bowen D. V., Lehner N., Sembach K. R., Thom C., Tumlinson J., 2011, Science, 334, 952

Tripp T. M., Savage B. D., Jenkins E. B., 2000, The Astrophysical Journal Letters, 534, L1

Tripp T. M., Sembach K. R., Bowen D. V., Savage B. D., Jenkins E. B., Lehner N., Richter P., 2008, ApJS, 177, 39

Verner D. A., Barthel P. D., Tytler D., 1994, A&AS, 108, 287

Weinberg D. H., Miralda-Escude J., Hernquist L., Katz N., 1997, ApJ, 490, 564

Wiersma R. P. C., Schaye J., Smith B. D., 2009a, MNRAS, 393, 99

Wiersma R. P. C., Schaye J., Theuns T., 2011, MNRAS, 415, 353

Wiersma R. P. C., Schaye J., Theuns T., Dalla Vecchia C., Tornatore L., 2009b, MNRAS, 399, 574

Williger G. M., Heap S. R., Weymann R. J., Davé R., Ellingson E., Carswell R. F., Tripp T. M., Jenkins E. B., 2006, ApJ, 636, 631

APPENDIX A: CURRENT STATUS OF Ne VIII OBSERVATIONS AT LOW REDSHIFT

In this section we give a summary of the *intervening* Ne VIII absorbers detected at low redshift and reported in the literature to date. So-called 'proximate' Ne VIII absorbers, which are believed to originate in the outflows of QSOs, have been also identified at low redshift (e.g. Muzahid et al. 2012), but they are out of the scope of this study.

The first Ne VIII absorber (with a total column density $\log_{10}(N_{\text{Ne VIII}}/\text{cm}^{-2}) = 13.85$ and corresponding rest-frame equivalent width $W_r \approx 33 \text{ m}\text{\AA}$) was discovered by Savage et al. (2005) at $z = 0.207$ along the sightline to the QSO HE 0226-4110 ($z_{\text{em}} = 0.495$) in a combined FUSE / STIS spectrum with $S/N = 10 - 20$ per resolution element. Absorption by H I and low ionisation states of other elements (e.g. C III, N III, Si III) and highly ionised oxygen (O VI) were also detected at the same redshift. While the low ionisation states could be explained by photo-ionisation, the same model failed to explain the observed O VI - Ne VIII absorption. The implied path length (~ 10 Mpc), in particular, would result in a Hubble broadening which is 10 times larger than the observed line width. Savage et al. (2005) thus concluded that the O VI - Ne VIII absorption is produced by collisionally ionised gas at a temperature $\log_{10}(T/\text{K}) \approx 5.7$. They estimated a total hydrogen column density $\log_{10}(N_{\text{H}}/\text{cm}^{-2}) \approx 20$ for this gas phase, suggesting that Ne VIII absorbers may harbour a significant fraction of the baryons in the Universe at low redshift. This absorption system was re-observed by Savage et al. (2011) in a COS spectrum of the source HE 0226-4110 with $S/N = 20 - 40$. With the Ne VIII absorption out of the COS spectral range at this redshift, this group focused on the detection of a feature identified as a broad Ly α absorber (BLA) with $\log_{10}(N_{\text{H}}/\text{cm}^{-2}) \approx 13.9$ and a Doppler parameter $b_{\text{Ne VIII}} = 72_{-6}^{+13} \text{ km s}^{-1}$, consistent with gas at a temperature in the range $\log_{10}(T/\text{K}) = 5.4 - 5.7$. A joint model of the BLA - O VI - Ne VIII system allowed them to constrain the temperature to $\log_{10}(T/\text{K}) = 5.68 \pm 0.02$ and the total hydrogen column density to $\log_{10}(N_{\text{H}}/\text{cm}^{-2}) = 20.06 \pm 0.09$, thus reinforcing the conclusion by Savage et al. (2005) that Ne VIII absorbers at low redshift contain a significant amount of baryons.

A second Ne VIII detection ($\log_{10}(N_{\text{Ne VIII}}/\text{cm}^{-2}) = 13.98$, $W_r = 47 \text{ m}\text{\AA}$) at $z = 0.326$ was reported by Narayanan et al. (2009). This absorber was identified in a FUSE spectrum of the QSO 3C 263 ($z_{\text{em}} = 0.646$) with $S/N = 5 - 10$. This group found that the ionisation state of the gas phase giving rise to the observed Ne VIII absorption could not be explained by photo-ionisation. Rather, this absorber appears to be multi-phase, with the Ne VIII absorption arising in gas at $T \sim 10^6 \text{ K}$. These authors provided the first estimate of the baryonic content of Ne VIII systems, $\Omega_b(\text{Ne VIII}) = 0.00263$, which corresponds to roughly 6 per cent of the total baryons in the Universe (assuming $\Omega_b = 0.0418$). This absorber was later confirmed in a COS spectrum by Narayanan et al. (2012). They re-analysed the physical conditions in this O VI - Ne VIII absorbing gas, and found that it is best modelled with gas in CIE at $T = 5.2 \times 10^5 \text{ K}$ with $[\text{Ne}/\text{H}] = -0.12_{-0.18}^{+0.12}$ (adopting $(n_{\text{Ne}}/n_{\text{H}})_{\odot} = -4.07$). These authors noted for the first time the surprisingly small number of Ne VIII detections at low redshift⁹. This fact led to the interpretation that the Ne VIII absorbers have a physical origin different from the filamentary structures of the highly ionised gas outside the virial

⁹ For comparison, there are more than 100 O VI detections at low redshift reported in the literature to date (see e.g. Tilton et al. 2012).

boundaries of galaxies. This group suggested that the observed Ne VIII absorption originates in the extended regions around galaxies, i.e. the circum-galactic medium (CGM), which is consistent with the relatively high metal abundances of the Ne VIII absorbers.

Narayanan et al. (2011) next reported on the detection of absorption by Ne VIII (and associated O VI) in an intervening, multi-phase system at $z = 0.495$ in a COS spectrum ($S/N = 15 - 20$) along the sightline to the source PKS 0405-123. Using the apparent optical depth method (AOD; Savage & Sembach 1991), they measured $\log_{10}(N_{\text{Ne VIII}}/\text{cm}^{-2}) = 13.96$ and $W_r = 45 \text{ m}\text{\AA}$. Allowing for the observed O VI to have a significant contribution from the photo-ionised, cooler gas phase, the ionisation state of the warmer, O VI - Ne VIII absorbing phase can be explained with a model that takes into account both photo- and collisional ionisation. Adopting a fixed temperature $T = 4.7 \times 10^5 \text{ K}$ and $[\text{Ne}/\text{H}] = -0.3$ (relative to $(n_{\text{Ne}}/n_{\text{H}})_{\odot} = -4.07$), Narayanan et al. (2011) estimated a gas density $n_{\text{H}} \approx 8 \times 10^{-4} \text{ cm}^{-3}$, and a linear size of the absorber of roughly 20 kpc.

Another prominent example is the system in a COS spectrum of the QSO PG 1206+459 reported by Tripp et al. (2011). This group detected a strong, complex Ne VIII absorber (and absorption by a series of other high and low ionisation states of other elements: H I; Mg II, Mg X; N II, N III, N IV, N V; O III, O IV; S III, S IV, S V) at $z = 0.927$, consisting of nine individual components with a total column density $\log_{10}(N_{\text{Ne VIII}}/\text{cm}^{-2}) \approx 14.9$. They found strong evidence that the Ne VIII absorption is produced by the highly enriched, kinematically complex plasma in a strong outflow from a post-starburst galaxy ($L = 1.8 L^*$) at $z = 0.927$ and a projected impact parameter $\rho = 68 \text{ kpc}$ from the sightline. They estimated that the warm-hot ($T > 10^5 \text{ K}$) gas phase contains 10 - 150 times more mass than the cool ($T < 10^5 \text{ K}$) photo-ionised gas phase, with individual absorbing components harbouring $10^8 M_{\odot} - 4 \times 10^{10} M_{\odot}$.

Finally, three intervening systems at $z = 0.684$, 0.705 , and 0.725 along a single sightline to the QSO PG 1148+549 containing Ne VIII (and O VI) were reported by Meiring et al. (2012). These absorbers were detected in a COS spectrum with $S/N = 20 - 40$. Two of the absorbers ($z = 0.684$, $z = 0.705$) appear to be two-component systems, with total $\log_{10}(N_{\text{Ne VIII}}/\text{cm}^{-2}) = 13.95$ and $W_r \approx 43 \text{ m}\text{\AA}$, and total $\log_{10}(N_{\text{Ne VIII}}/\text{cm}^{-2}) = 13.86$ and $W_r \approx 35 \text{ m}\text{\AA}$, respectively. The system at $z = 0.725$ shows a very simple kinematic structure (probably single-component) with $\log_{10}(N_{\text{Ne VIII}}/\text{cm}^{-2}) = 13.81$ and $W_r \approx 33 \text{ m}\text{\AA}$. All three O VI - Ne VIII absorbers can be explained as being produced in gas in CIE with a temperature around $\log_{10}(T/\text{K}) = 5.7$, and a metallicity (i.e. oxygen abundance) $[\text{O}/\text{H}] > -0.5$. Assuming the O VI - Ne VIII absorption is produced in the CGM of galaxies, and using the observed absorber redshift density and the galaxy luminosity function, Meiring et al. inferred an average size of 70 - 150 kpc for typical O VI - Ne VIII absorbers at $z = 0.7$. This group further estimated that the density of gas as traced by these absorbers is $\Omega_b = 0.002$, or roughly 4 per cent of the baryon density (assuming $\Omega_b = 0.0418$).

APPENDIX B: SYNTHETIC SPECTRA

The Ne VIII line statistics (Section 2.1.2) and the Ne VIII- and H I-optical depth weighted quantities used throughout this work have been extracted from a set of spectra along 5000 random sightlines drawn from our simulation at $z = 0.5$, filling a total redshift path $\Delta z = 212$, corresponding to an absorption path length $\Delta\chi = 387$. For each sightline we have computed a pair of synthetic spectra,

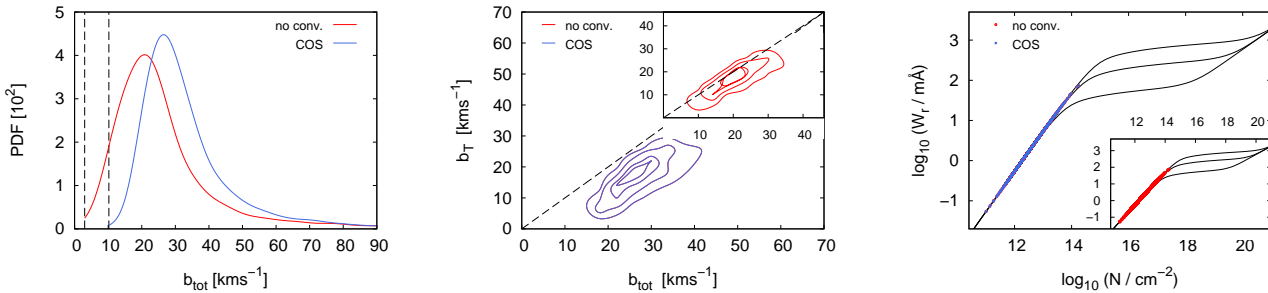


Figure A1. *Left:* Distribution of Doppler parameters of the Ne VIII components. The dashed vertical line indicate in each case the resolution limit, i.e. the minimum adopted b -value. The blue line show the distribution of components identified in spectra that have been convolved with a Gaussian LSF ($FWHM = 17 \text{ km s}^{-1}$), while the red line shows the distribution of components identified in spectra that have *not* been convolved. *Centre:* Comparison of the total line width, $b_{\text{Ne VIII}}$, to the thermal line width, b_T (equation 9) of the *single-component* Ne VIII components identified in high-S/N spectra in our simulation at $z = 0.5$. Clearly, the *intrinsic* width of the absorption lines is mainly set by temperature of the absorbing gas. However, convolution with an instrumental LSF results in absorption lines that are broader with respect to the pure thermal line width. Note that roughly half (45 per cent) and one third (35 per cent) of the Ne VIII absorbers appear as single-component features in the convolved and non-convolved spectra, respectively. *Right:* Rest-frame equivalent width and column density for our sample of Ne VIII absorbing components identified in 5000 spectra along random sightline drawn from our simulation at $z = 0.5$; each of the black curves shows a theoretical curve-of-growth (CoG) adopting $b_{\text{Ne VIII}} = 50 \text{ km s}^{-1}$, 18 km s^{-1} , and 4 km s^{-1} (from top to bottom). Meaning of colours identical to the left panel. Note that there is a linear relationship between equivalent width and column density for all Ne VIII components. Since equivalent width is conserved, convolution with an instrumental LSF does not affect the measured column density.

with each spectrum containing absorption by $\text{H I Ly}\alpha$ or Ne VIII 770.41 \AA only. These spectra have been generated using the package SPECWIZARD written by Joop Schaye, Craig M. Booth, and Tom Theuns, following the method described in detail in Tepper-García et al. (2011, their Section 3.1). We have convolved our spectra with a Gaussian line-spread function (LSF) with a $FWHM = 17 \text{ km s}^{-1}$, and have re-sampled our spectra onto pixels of 3 km s^{-1} in size, which roughly match the instrumental properties of COS. Finally, we have added Gaussian noise with a flux dependent root-mean-square (rms) amplitude given by $(\text{S}/\text{N})^{-1} F(v)$, where $F(v)$ is the flux as a function of velocity along the sightline, and S/N is the adopted signal-to-noise ratio; we adopt $\text{S}/\text{N}=1000$ to allow for the detection of most of the Ne VIII in our simulation (see below and Section 2.2). Throughout this work, we shall refer to these as 'high-S/N, COS-like' spectra.

We fit our synthetic spectra using a significantly modified version of AUTOVP (Davé et al. 1997) following the method detailed in Tepper-García et al. (2012, their Appendix A). Briefly, Ne VIII absorption lines are identified in regions with an (integrated) rest-frame equivalent width $W_r \geq N \sigma_{W_r}$, where σ_{W_r} is the uncertainty in the equivalent width, integrated over n pixels, and N is the significance level. We adopt $n = 25$ (equivalent to 75 km s^{-1} or approximately four times our adopted spectral resolution) and¹⁰ $N = 5$. With these values, the significance value chosen translates into a formal, rest-frame equivalent width limit $W_r \approx 193 (\text{S}/\text{N})^{-1} \text{ m}\text{\AA}$. This implies a *formal* completeness limit $W_r \approx 0.2 \text{ m}\text{\AA}$ or $\log_{10}(N_{\text{Ne VIII}}/\text{cm}^{-2}) \approx 11.5$ for our spectra with $\text{S}/\text{N}=1000$. To ensure the detection of all relevant features, we impose a minimum column density $\log_{10}(N_{\text{Ne VIII}}/\text{cm}^{-2}) = 11.0$, which is a factor 3 below the formal completeness limit. We note that the effective completeness limit is somewhat higher, $\log_{10}(N_{\text{Ne VIII}}/\text{cm}^{-2}) \approx 11.7$ or $W_r \approx 0.3 \text{ m}\text{\AA}$.

Each component is fitted assuming a Gaussian profile,¹¹ and the parameters (velocity centroid v_0 , column density $N_{\text{Ne VIII}}$, and Dop-

pler parameter $b_{\text{Ne VIII}}$) of all lines identified in each region are simultaneously and iteratively adjusted using the Levenberg-Marquardt algorithm (Levenberg 1944; Marquardt 1963) as implemented in Press et al. (1992) until the reduced χ^2 -value, i.e. the χ^2 -value divided by the degrees of freedom, is below $\chi^2_{\text{th}} \equiv 1.25$. During each iteration, lines with relative errors in $N_{\text{Ne VIII}}$ or $b_{\text{Ne VIII}}$ larger than 50 per cent are discarded. Note that each region is fitted with the *least number of absorption components* consistent with the condition $\chi^2 \leq \chi^2_{\text{th}}$. Fitting of our 5000 simulated spectra yields a total of 8665 Ne VIII components, with roughly half (45 per cent) of the identified Ne VIII absorbers being single-component features. The total cumulative line frequency per unit redshift is $dN/dz(W_r > 0.3 \text{ m}\text{\AA}) \approx 41$.

To investigate the effect of the instrumental broadening on the line properties, we fit a second set of spectra which are identical to our COS-like spectra except that these new spectra are not convolved with an instrumental LSF. In Figure A1 we compare the line parameters of the two Ne VIII absorption lines samples obtained from these two different sets. The left panel demonstrates that convolution with a Gaussian LSF artificially increases the line width by a significant amount. Therefore, while the intrinsic line width is a good indicator of the gas temperature (central panel, inset), the width of lines identified in convolved spectra can at most provide an upper limit to the gas temperature. The right panel shows the relationship between rest-frame equivalent width and column density (i.e. the curve-of-growth). Clearly, the equivalent width of the majority of the Ne VIII absorbers depends linearly on the Ne VIII column density. Since the rest-frame equivalent width is conserved under a convolution, the column density of the lines is conserved as well.

¹⁰ The Ne VIII detections reported to date in the literature have a significance $N\sigma \gtrsim 4\sigma$.

¹¹ The column density of the lines are low enough that the difference between a Gaussian and a Voigt-Profile is negligible.